

Transient analysis of stall onset in highly-loaded tandem rotor configurations for an axial compressor

Kumar, Amit; Kumar, Akshay; Chhugani, Hitesh; Payyappalli, Manas; Pradeep, A. M.

DOI

[10.1063/5.0256513](https://doi.org/10.1063/5.0256513)

Publication date

2025

Document Version

Final published version

Published in

Physics of Fluids

Citation (APA)

Kumar, A., Kumar, A., Chhugani, H., Payyappalli, M., & Pradeep, A. M. (2025). Transient analysis of stall onset in highly-loaded tandem rotor configurations for an axial compressor. *Physics of Fluids*, 37(3), Article 036152. <https://doi.org/10.1063/5.0256513>

Important note

To cite this publication, please use the final published version (if applicable).
Please check the document version above.

Copyright

Other than for strictly personal use, it is not permitted to download, forward or distribute the text or part of it, without the consent of the author(s) and/or copyright holder(s), unless the work is under an open content license such as Creative Commons.

Takedown policy

Please contact us and provide details if you believe this document breaches copyrights.
We will remove access to the work immediately and investigate your claim.

Green Open Access added to TU Delft Institutional Repository




'You share, we take care!' - Taverne project

<https://www.openaccess.nl/en/you-share-we-take-care>

Otherwise as indicated in the copyright section: the publisher is the copyright holder of this work and the author uses the Dutch legislation to make this work public.

RESEARCH ARTICLE | MARCH 26 2025

Transient analysis of stall onset in highly-loaded tandem rotor configurations for an axial compressor

Amit Kumar (अमित कुमार)  ; Akshay Kumar (अक्षय कुमार); Hitesh Chhugani (हितेश छुगानी);
Manas Payyappalli (മാനസ് പയ്യപ്പള്ളി)  ; A. M. Pradeep (എ എം പ്രദീപ്) 



Physics of Fluids 37, 036152 (2025)

<https://doi.org/10.1063/5.0256513>



View
Online



Export
Citation

Articles You May Be Interested In

Aeroacoustic analysis of the tip-leakage flow of an ultrahigh bypass ratio fan stage

Physics of Fluids (April 2023)

Investigation of compressibility effects on dynamic stall of pitching airfoil

Physics of Fluids (July 2017)

Investigation of mechanisms on leading edge vortex generation and suppression in vaned diffuser of a centrifugal compressor

Physics of Fluids (September 2024)



Physics of Fluids

Special Topics Open
for Submissions

[Learn More](#)

Transient analysis of stall onset in highly-loaded tandem rotor configurations for an axial compressor

Cite as: Phys. Fluids **37**, 036152 (2025); doi: [10.1063/5.0256513](https://doi.org/10.1063/5.0256513)

Submitted: 5 January 2025 · Accepted: 6 March 2025 ·

Published Online: 26 March 2025



View Online



Export Citation



CrossMark

Amit Kumar (अमित कुमार),^{1,a)}  Akshay Kumar (अक्षय कुमार),² Hitesh Chhugani (हितेश छुगानी),²  Manas Payyappalli (മാനസ് പയ്യപ്പള്ളി),³  and A. M. Pradeep (എ എം പ്രദീപ്)² 

AFFILIATIONS

¹Department of Energy Conversion and Storage, Technical University of Denmark, Anker Engelunds Vej 1, Bygning 101A, 2800 Kongens Lyngby, Denmark

²Department of Aerospace Engineering, Indian Institute of Technology Bombay, Mumbai 400076, India

³Faculty of Aerospace Engineering, TU Delft, Kluyverweg 1, 2629 HS Delft, The Netherlands

^{a)}Author to whom correspondence should be addressed: kumaramt1986@gmail.com

ABSTRACT

High thrust-to-weight ratio is crucial in aero-engine design. The adverse pressure gradient in compressors limits the maximum diffusion per stage, necessitating more stages to achieve the desired pressure ratio. Tandem airfoils, with their superior diffusion capability compared to conventional single airfoils, can achieve the required pressure ratio with fewer stages. However, the presence of two tip leakage vortices from both the forward and aft rotors creates a more complex tip region compared to conventional rotors. The design and performance aspects of the tandem rotor have been reasonably well documented. However, the stall characteristics of such rotors are yet to be thoroughly investigated. To better understand the stall phenomenon in a tandem rotor, the role of each tip leakage vortex must be investigated separately. Full annulus unsteady analysis of the highly loaded tandem rotor is carried out using the commercially available software Ansys CFX. As the rotor approaches stall, significant changes occur in the trajectory and strength of these vortices, with increased blockage near the stall point. For the tandem rotor, forward rotor spillage is critical. This spillage increases the local incidence near the tip of the forward rotor, resulting in localized flow separation. Small disturbances arising from the leading-edge separation coalesce, forming a rotating stall cell that grows in strength and size as it rotates in the direction opposite to rotor rotation. Even though the aft rotor encounters tip vortex spillage from the forward and aft rotors of the subsequent passage, the nozzle gap effect effectively mitigates flow separation, ensuring stable operation of the tandem rotor system. The leading-edge separation over the forward rotor suction surface evolves into a tornado vortex, with the suction leg on the forward rotor suction surface and the other end connected to the casing. Apart from the tip leakage vortex of the aft rotor, other vortex structures on the aft rotor are intermittent, with some collapsing and new vortices forming.

Published under an exclusive license by AIP Publishing. <https://doi.org/10.1063/5.0256513>

I. INTRODUCTION

Modern aero-engine designs operate at very high-pressure ratios to maximize thermal efficiency and reduce specific fuel consumption, with some engines reaching pressure ratios as high as 50–60. Compressor designers face the challenge of achieving the required pressure ratio with fewer stages while maintaining efficient compression across a wide range of operating conditions. The work transfer to the incoming air, or compression, is proportional to both the rotational speed and the flow turning angle. Although airfoil shapes have evolved to become more efficient and suitable for high-speed applications, the maximum rotational speed is still limited by losses and maximum

allowable blade stress. Airfoils designed with higher flow turning are prone to flow separation. However, higher flow turning angles can be accomplished using tandem blading configurations, which have the potential to provide greater diffusion than conventional designs. Unlike traditional single airfoils, tandem blades use two smaller airfoils—the forward and aft blades—creating a nozzle-like shape between them. This design effectively controls boundary layer growth over the aft airfoil, preventing early flow separation. Thus, the tandem configuration has the potential to achieve the required pressure ratio with fewer stages, thereby shortening the overall engine length and increasing specific thrust.

Figure 1 shows the schematic of a typical tandem blade configuration. The axial overlap (AO) and percentage pitch (PP) directly govern the relative positioning of the forward and aft rotors and the type of nozzle formed between them. Axial overlap controls the axial shift, while percentage pitch determines the tangential shift of the aft rotor. Several experimental and numerical studies have explored the design and aerodynamic aspects of tandem configurations. Tandem configurations have exhibited better diffusion characteristics than conventional single-blade configurations.^{1–6} The performance of tandem blades is mainly influenced by the nozzle formed between the two blades, which depends on the aft blade's position relative to the forward blade. Optimal performance in tandem blade configurations is achieved with a higher percentage pitch (PP) and lower axial overlap (AO).^{4–6} However, tandem performance degrades due to inadequate momentum transfer through the gap nozzle during off-design conditions.⁷ Researchers have further studied the effect of loading distribution between the forward and aft blades, finding that blade loading should be evenly distributed between the two blades for optimal performance. The chord ratio between the forward and aft blades also significantly influences tandem rotor performance. Cascades with longer front blade chords demonstrated higher operating ranges than other configurations.⁸ Other studies have shown that end wall losses for tandem blades are lower compared to conventional blades, resulting in better performance.^{9,10}

The effect of inlet flow distortion on a tandem rotor has also been explored, showing that distortion significantly reduces the stall margin, primarily due to higher tip loading.^{6,11} Furthermore, the study highlighted that the tandem rotor is highly sensitive to forward rotor tip clearance,¹² and the front blade significantly influences overall performance.¹³ The tip sensitivity of tandem rotors can be reduced by integrating lean, sweep, and dihedral. Integrating negative lean and forward chordwise sweep significantly improves the stall margin.¹⁴

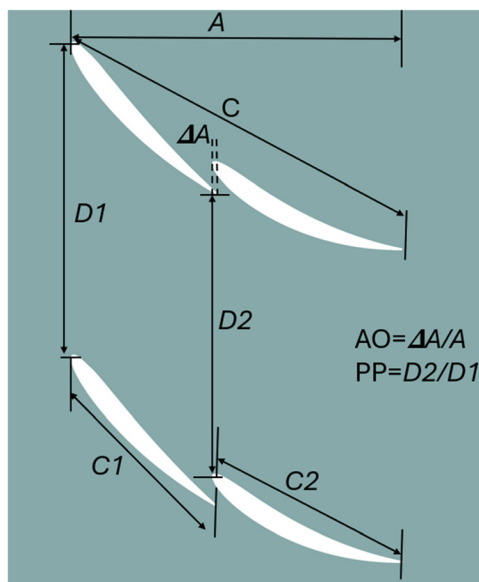


FIG. 1. Schematic of tandem rotor.

Other researchers^{15,16} have also explored the flow dynamics within tandem configurations.

In summary, previous studies have highlighted the potential of tandem rotor configurations to provide better diffusion characteristics than conventional rotors. However, their performance tends to degrade more significantly under off-design conditions. Due to the presence of twin tip leakage vortices, the tip region of tandem rotors is more complex and tip-sensitive compared to that of conventional rotors. Incorporating three-dimensional blade designs can help to reduce this tip sensitivity. Despite these advancements, several aspects of tandem rotor design still require further exploration before they can be fully integrated into practical applications. In particular, the unsteady behavior and stall inception of tandem rotors remain unexplored, even though understanding these aspects is crucial for their successful implementation.

Stall is a critical phenomenon in compressors, characterized by disturbances that disrupt the smooth flow of air, leading to performance degradation and potential damage to the engine. Understanding these stall phenomena is paramount for compressor design and stability. The stall phenomenon in conventional rotors is well-documented.

Several experimental and numerical studies have established tip leakage as the primary driver of rotating instability in axial compressors.^{17–30} With zero tip clearance, corner separation blockage drives the rotor toward the stall. The unstalled flow range first extends as tip clearance increases from zero tip clearance, but eventually, tip leakage flow dominates, consequently reducing the stall range.¹⁷ Additionally, tip leakage vortex is the primary reason for spike-type compressor rotating stall.^{17–20} Studies revealed that the spike originates from leading-edge separation, causing vorticity to shed and a vortex to form between the suction surface and the casing. These vortices move toward the pressure surfaces of adjacent blades, triggering separations and causing the spike to propagate. Two key conditions for the onset of spike rotating stall disturbances are the interface between tip leakage and oncoming flows becoming parallel to the leading-edge plane and the initiation of backflow at the trailing-edge plane from adjacent passages.¹⁹

Yamada *et al.*²⁰ studied the unsteady behavior and three-dimensional flow structure of spike-type stall inception in an axial compressor rotor using both experimental and numerical methods. The results demonstrated a low-pressure region traveling circumferentially near the leading edge, detected shortly after a spike in casing wall pressure. Numerical simulations using detached-eddy simulation (DES) revealed that this low-pressure region is caused by a tornado-like separation vortex from a leading-edge separation near the rotor tip. This vortex connects the blade suction surface to the casing wall and moves circumferentially. When it interacts with the next blade's leading edge, the separation propagates, leading to stall and reduced compressor performance. Similarly, Wang *et al.*,²¹ Chen *et al.*,²² Khaleghi,²³ and others^{24–28} have corroborated these findings, emphasizing the significance of tip leakage in driving rotating instability. The part-span rotating stalls in high-speed axial flow compressors have also been explored. Dodds and Vahdati²⁹ identified two families of rotating stalls, high and low frequency, by deliberately mismatching the front stages with variable stator vanes, corresponding to high and low cell counts, respectively. Their subsequent study³⁰ utilized 3D unsteady RANS simulations to delve into the physical aspects of these

phenomena. The simulations revealed two distinct stall patterns: one originating from hub corner separations on stage 1 stator vanes, creating a multicell pattern in the hub region, and the other from tip clearance flow over stage 1 rotor blades, resulting in a multicell pattern in the leading-edge tip region.

In rotating wings,³¹ dynamic stalls occur when high angles of attack combine with rapid angle changes in the angle of attack, leading to flow separation. This unsteady phenomenon involves complex interactions of different vortices. Unsteady flow behavior can be observed over a sphere, where vortex shedding and the dynamics of flow separation play a key role in flow instability.³² Dynamic stall is also relevant to fixed wings, flapping wings, wind turbines, and similar systems.³³ In all these configurations—compressor, rotating wings, fixed wings, flapping wings, and wind turbines—stall is attributed to higher angles of attack and is characterized by complex, unsteady phenomena driven by interactions of vortices and flow instabilities.

Past researchers have extensively studied various design and performance aspects of tandem rotors. However, the unsteady behavior of tip leakage vortices and their critical role in stall inception remain unexplored in the open literature. This study addresses this gap by focusing on the unsteady dynamics of tip leakage vortices in tandem rotors and their contribution to the stall inception process, providing novel insights into tandem rotor behavior. While the stall phenomenon in conventional rotors has been widely investigated, the characterization of stall in tandem rotors has not been investigated so far. Conventional rotors typically follow either modal or spike-type stall mechanisms, but this pathway has not yet been established for tandem rotors. The tandem rotor's tip region is inherently more complex due to the presence of twin leakage vortices. The tip leakage vortices of the forward and aft rotors differ in trajectory and strength. Furthermore, the flow near the stall is dominated by unsteady interactions and the formation of various vortex structures, which further complicate the dynamics. Previous research on conventional rotors has identified tip leakage as a primary driver of rotating instability. To fully understand the stall phenomenon in tandem rotors, it is essential to separately examine the role of each tip leakage vortex. To the best of the authors' knowledge, this is the first attempt in open literature to characterize the stall behavior of a tandem rotor. This paper aims to achieve the following objectives:

1. Characterize and investigate the stall inception in a highly loaded tandem rotor.
2. Understand the distinct roles and behaviors of the forward and aft tip leakage vortices.
3. Identify the impact of each tip leakage vortex on the stall phenomenon.

The structure of this paper begins with a section on design and computational details, describing the numerical methods, mesh generation, boundary conditions, and other relevant parameters. The section also briefly covers the validation of the computational fluid dynamics (CFD) model by comparing numerical results with experimental data. In the results and discussion section, the first part provides a comprehensive analysis of stall inception in tandem rotors, focusing on the roles of the forward and aft tip leakage vortices. The second part thoroughly examines unsteady pressure data from casing sensors using Fourier analysis and a novel feature algorithm to identify stall cell behavior and propagation.

TABLE I. Design specification of tandem rotor.

Specification	
Total pressure rise coefficient, ψ_{mean}	1.21
Design mass flow rate, m_d	6 kg/s
Design RPM	2700
Hub to tip ratio	0.5
Hub diameter	250 mm
DF_{tip} , DF_{mean} , DF_{hub}	0.64, 0.63, 0.49
Number of forward rotor blade	19
Number of aft rotor blades	19
Chord of forward and aft rotor	41 mm, 41 mm
Airfoil	C4

II. DESIGN, COMPUTATIONAL DETAILS, AND CFD VALIDATION

Tables I and II list the design details of the tandem rotor.⁶ The tandem rotor is designed for low-speed applications with a design rotational speed of 2700 rpm. The design mass flow rate and pressure rise coefficient are 6 kg/s and 1.21, respectively. The tandem rotor was designed for a high flow turning angle. The tandem rotor comprises 19 forward and 19 aft blades. The hub-to-tip ratio is 0.5, and the tip diameter is 500 mm. The design tip gap is 0.72% of the blade length. To initiate the stall and create the asymmetry of flow, the tip gap of one forward rotor and one aft rotor is increased to 1.2% of the blade length [marked by the black dotted box in Fig. 2(a)]. Therefore, in a full annulus study, the tip gap of 18 forward and 18 aft rotors is 0.72% of the blade length, while the tip gap of one forward and one aft rotor increases to 1.2% of the blade length.

Figure 2(a) shows the fluid domain of the full annulus simulation. The inlet domain is positioned 375 mm upstream of the forward rotor leading edge, while the outlet domain is positioned 500 mm downstream of the aft rotor trailing edge. To trace and identify the nature of the stall cell, 1000 monitor points are created near the casing. Pressure and velocity data are recorded at ten axial positions (−10%C, 0%C, 14%C, 28%C, 42%C, 56%C, 72%C, 88%C, 100%C, 108%C). At each axial location, 100 equidistant monitor points span the full annulus. Thus, there are 100 numerical probes distributed evenly around 360° to capture the behavior of the stall cell at each axial location. Figure 2(b) shows a schematic of these numerical probes. Figure 3 illustrates the mesh in various sections of the rotor domain. The hexahedral mesh is generated using Turbogrid,³⁴ with a very fine mesh

TABLE II. Design specification of forward and aft rotor at different spans.

D/D_t	Forward rotor				Aft rotor			
	ψ	γ	θ	DF	ψ	γ	θ	DF
0.5	0.40	29.70	27.66	0.41	0.40	0.87	45.90	0.34
0.6	0.49	37.51	24.25	0.44	0.49	11.33	43.96	0.44
0.7	0.57	44.10	21.34	0.45	0.57	21.53	39.70	0.50
0.8	0.66	49.56	19.16	0.46	0.66	30.70	34.87	0.52
0.9	0.75	54.06	17.70	0.46	0.75	38.52	30.57	0.54
1	0.83	57.33	17.11	0.46	0.83	44.01	27.71	0.55

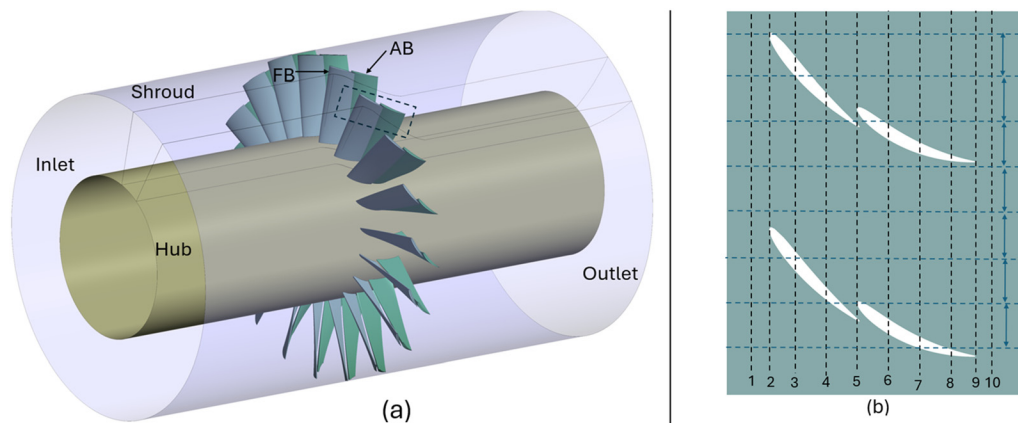


FIG. 2. Computational domain of tandem rotor for full annulus study. (a) Fluid domain. (b) Monitor points.

around the blade surface, hub, and shroud. To accurately capture the tip leakage phenomena, 17 elements are placed inside the tip gap. The minimum skewness is around 22° , and wall y^+ is approximately 1. Approximately 36.7×10^6 elements are used for the full annulus unsteady simulation.

The full annulus transient simulations are carried out using the commercial software Ansys CFX,³⁴ which solves the Reynolds averaged Navier–Stokes equations for mass, momentum, and energy within a finite volume framework using a fully coupled pressure-based approach.³⁴ In the simulations, air is considered a perfect gas mixture. The solver employs an implicit scheme for numerical calculations and a central difference scheme for discretization. Turbulence is modeled using the Shear Stress Transport (SST) $k-\omega$ model, which solves the Reynolds stress terms using turbulent kinetic energy (k) and specific rate of dissipation (ω).³⁴ The SST $k-\omega$ is known for its superior

performance in predicting flow separation, making it ideal for investigating stall in this case. Additionally, the SST $k-\omega$ model shows better validation with experimental results compared to other turbulence models available in Ansys CFX.

For the transient simulation, each blade passage is divided into 20 parts. In each time step, the rotor rotates approximately 0.95° . Given the rotational speed, the time step is 5.84795×10^{-5} s. In the unsteady simulation, each iteration is assigned 15 inner iterations. This value is determined based on convergence criteria. An adequate number of inner iterations ensures satisfactory convergence, as insufficient iterations may lead to unsatisfactory or inaccurate results. Conversely, assigning a higher number of inner iterations would unnecessarily increase computational time without any significant improvement in accuracy. Therefore, 15 inner iterations were chosen as an optimal balance between accuracy and computational efficiency. Completing one

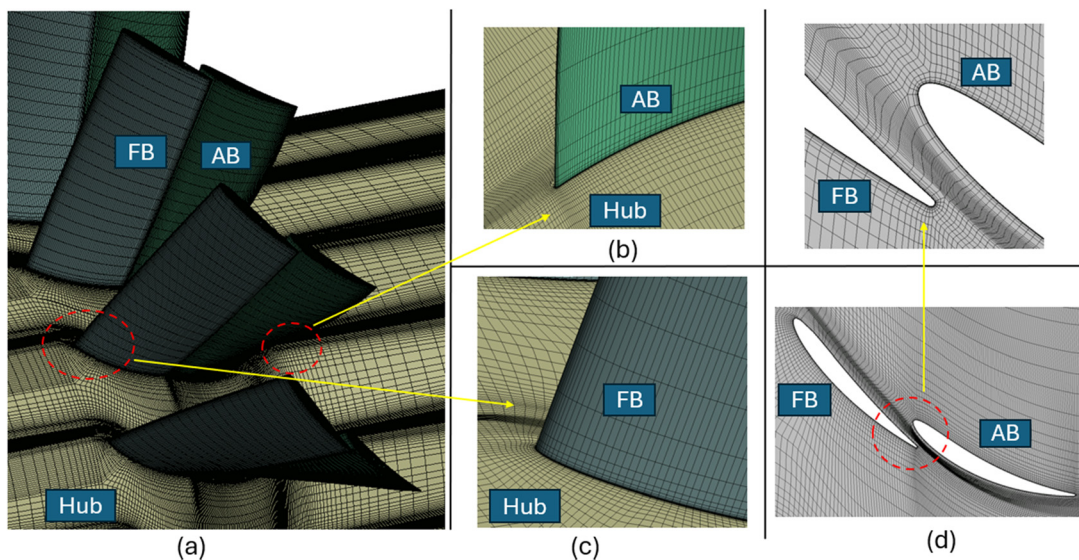


FIG. 3. Mesh. (a) Inside rotor domain. (b) Near trailing edge. (c) Near leading edge. (d) In nozzle-gap.

rotor revolution requires 380-time steps. The high-resolution scheme is used for mass, momentum, and energy, while the upwind scheme is used for turbulence. For transient simulation, the second-order backward Euler scheme is used. The SST $k-\omega$ turbulence model, known for capturing flow separation more effectively than the $k-\varepsilon$ turbulence model, is used for the simulation. Experimental results of the tandem rotor were compared with the numerical simulations, showing better agreement with the SST $k-\omega$ model. Therefore, this model is utilized for further analysis.

For the unsteady simulation, a systematic approach is employed. Initially, a full annulus steady-state simulation is performed at the design mass flow rate. For the full annulus steady simulation, total pressure or total temperature is imposed at the inlet, while the mass flow rate is specified at the outlet. These results serve as the initial conditions for the subsequent steady analysis conducted near stall. This process continues until the mass flow rate is reached, where the solution diverges. The transient analysis begins with the steady-state solution from the full annulus simulation. Near the stall point, to accurately capture stall inception, the mass flow rate is gradually reduced in extremely small steps during the unsteady simulation. This

gradual reduction ensures a smooth transition and maintains stability throughout the simulation process.^{17–26} The full annulus transient simulation is conducted for more than 13 rotor revolutions. This period allowed the rotor to transition from the early stages of stall inception to the formation of fully developed stall cells.

Figure 4(a) illustrates the grid independence study. The grid independence study is conducted for a single passage at the design flow coefficient. Once grid convergence is achieved, the changes in the pressure rise coefficient become negligible. Based on this study, approximately 36.7×10^6 elements were used for the transient analysis to capture the relevant flow physics with sufficient resolution. Figures 4(b)–4(d) compare numerical results with experimental data of the tandem rotor. The experiment was carried out in the Turbomachinery Research Laboratory (TRL) at the Indian Institute of Technology Bombay.^{6,11,12,14} The single-stage axial compressor rig was designed for the low-speed application. To measure the total pressure rise across the tandem rotor, three Pitot probe rakes are positioned 1.5 chords upstream of the rotor leading edge, and four Kiel probes are placed 0.5 chords downstream of the aft rotor trailing edge. Additionally, a seven-hole probe is used to capture the radial profile at the exit. CFD

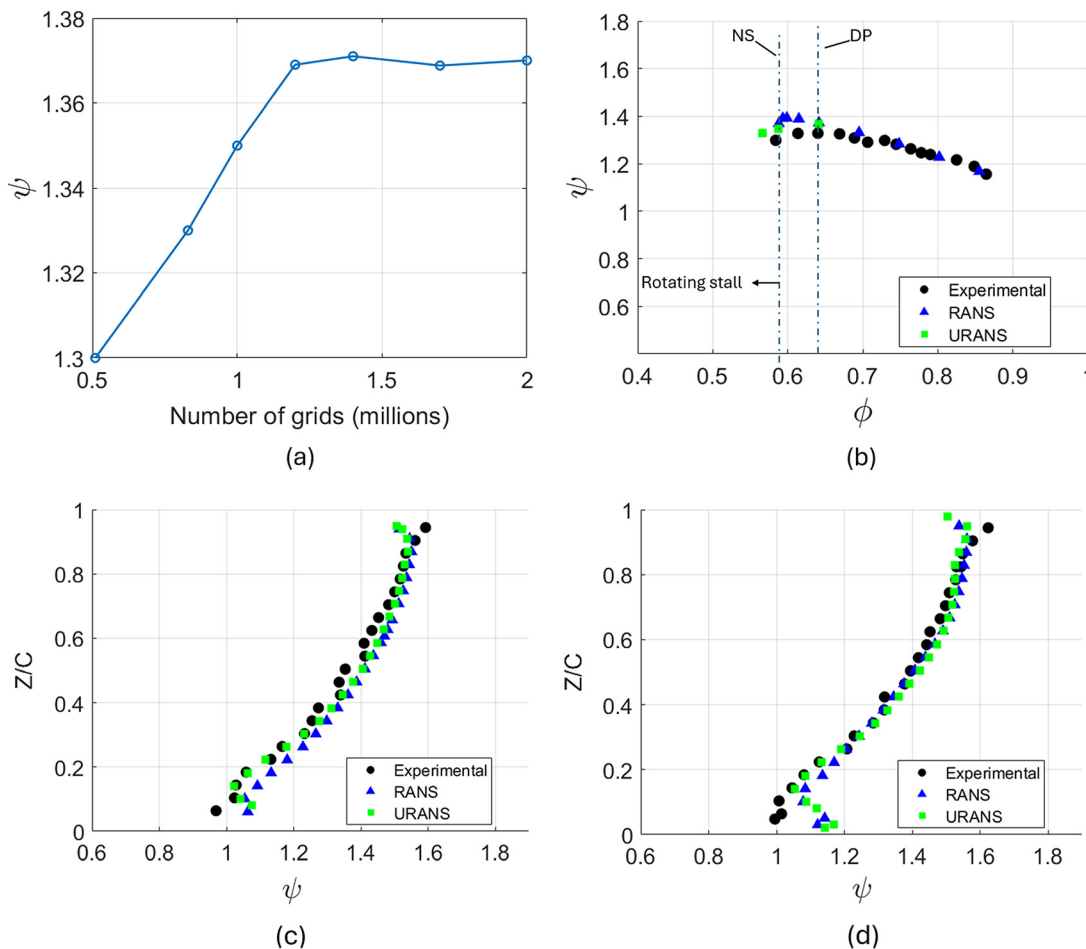


FIG. 4. Validation of the numerical model. (a) Grid independence study. (b) Comparison of performance map. (c) Comparison of radial total pressure profile near design point, DP. (d) Comparison of radial total pressure profile near stall, NS.

predictions align closely with experimental results. At the design point, discrepancies are within 2.1% for the RANS analysis. The difference between RANS and URANS near the design point is insignificant. The maximum discrepancy between the experimental and RANS numerical data occurs near the stall point but remains within 4%. This difference is further reduced to below 2.85% with the use of URANS.

Figures 4(c) and 4(d) compare the spanwise distribution of total pressure for RANS and URANS near the design and stall points, respectively. The total pressure increases from the hub toward the tip, which is consistent with the design methodology. The experimental spanwise data were obtained using a seven-hole probe, which was traversed from tip to hub to measure the total pressure at the rotor exit. The seven-hole probe has an angular sensitivity of $\pm 65^\circ$. Both RANS and URANS demonstrate excellent agreement with the experimental values at the design point, with minor deviations observed near the hub.^{6,11,12,14} However, these deviations increase near the stall point, although the overall trend remains well-matched. The total pressure profile remains nearly constant from the design to the stall point. Close examination of the RANS and URANS results reveals the formation of a horseshoe vortex near the hub due to boundary layer effects, causing an abrupt change in total pressure near the hub. The strength and interaction of this boundary layer vortex intensify near the stall. These effects, however, are not accurately captured by the seven-hole probe. The seven-hole probe, despite being a versatile tool for three-dimensional flow measurement, has inherent limitations near the wall. The finite tip size and strong interface restrict its ability to resolve small-scale flow features close to the wall. Despite these limitations, the experimental data closely align with the numerical predictions, validating the accuracy of the numerical methodology adopted in this paper. This agreement reinforces confidence in the robustness of numerical approaches used to model the flow physics.

III. RESULT AND DISCUSSION

A. Flow evolution from design point to near stall point

Figure 5 shows the entropy and axial velocity contours at 98% span, emphasizing the losses near the tip region at two different flow

coefficients ($\phi = 0.64$ and $\phi = 0.58$). This illustration highlights the changes occurring as the flow transitions from the design mass flow rate ($\phi = 0.64$) toward stall conditions. Regions of higher entropy indicate the formation of tip leakage vortices. The pressure difference between the pressure and suction sides of the forward and aft blades causes fluid to leak over the blade tip, interacting with the main flow and forming forward and aft tip leakage vortices. The strength of these vortices is proportional to the pressure differential across the tips of the forward and aft rotors. These vortices consume energy from the main flow, reducing its kinetic energy. The resulting turbulence and mixing from the forward and aft tip leakage vortices further decrease axial velocity. At the design point, the effect of a higher tip gap is confined to the adjacent blade passage. At lower mass flow rates, there are significant changes in both the trajectory and strength of the tip leakage vortices. Negative axial velocity at 98% span highlights the blockage. Near the stall point, the blockage caused by these vortices increases significantly. Compared to other blades, those with a higher tip gap exhibit higher blockage and loss regions.

Figure 6 shows the streamlines near the tip region at two different flow coefficients ($\phi = 0.64$ and $\phi = 0.58$). The streamlines near the tip region reveal the interaction between the tip leakage vortices of blades with a higher tip gap (marked with a black dotted box) and the subsequent blades. Forward and aft rotors of two blade passages have different tip clearances, leading to vortices with varying strengths and orientations. The effect of higher clearance is evident at both mass flow rates. The axial momentum of the main flow reduces near the stall point. The tangential momentum of the forward tip leakage vortices (TLV1) and aft tip leakage vortices (TLV2) dominates the axial momentum, therefore aligning more in the tangential direction. This holds true for all blades. Due to the different courses of movement, both tip leakage vortices interact immediately, creating a larger negative velocity region near the stall point. Vortex breakdown^{12,35–37} is particularly notable near stall or even at the design mass flow rate for the rotor with a higher tip gap.¹² This leads to increased blockage and associated losses, driving the rotor to stall.

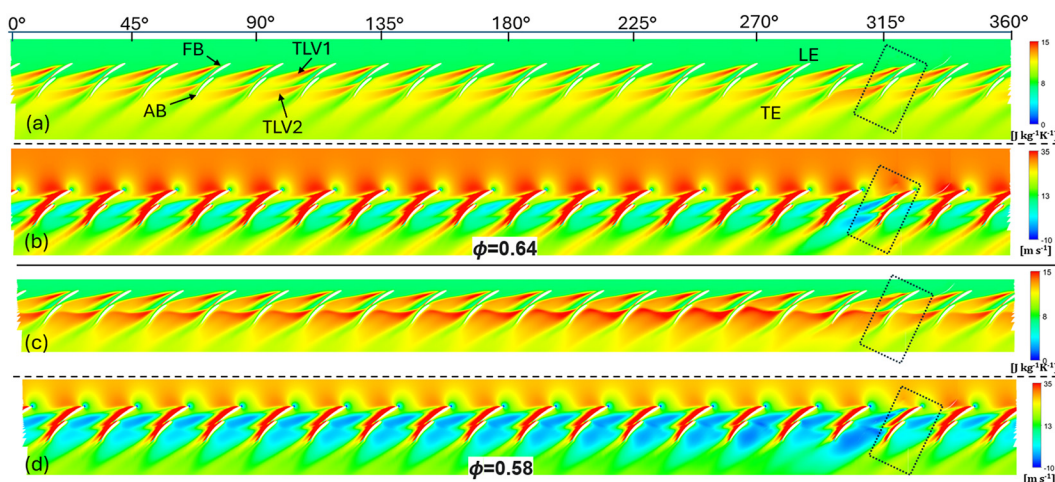


FIG. 5. Entropy and axial velocity at 98% span. (a) Entropy at $\phi = 0.64$. (b) Axial velocity at $\phi = 0.64$. (c) Entropy at $\phi = 0.58$. (d) Axial velocity at $\phi = 0.58$, blade with a higher tip gap marked with black dotted box.

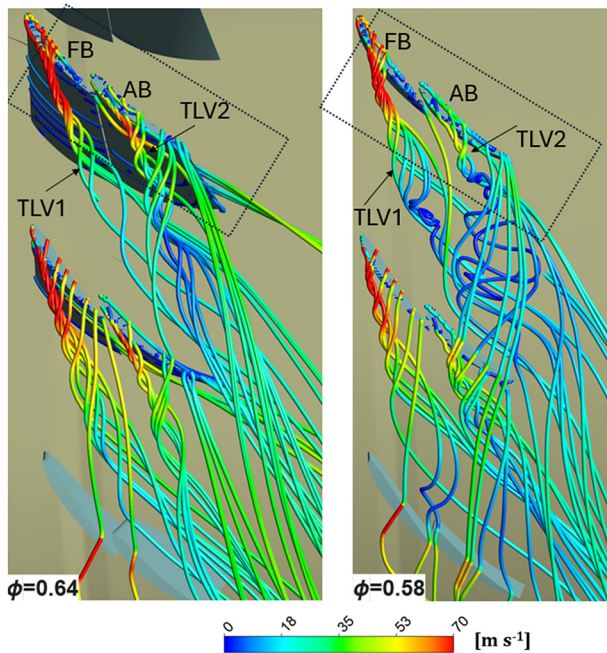


FIG. 6. Tip leakage streamlines at $\phi = 0.64$ and $\phi = 0.58$, blade with a higher tip gap marked with black dotted box.

B. Transient analysis of stall initiation and development

This section discusses the transient results, focusing on the evolution of the flow field near the tip region. Figure 7 displays the instantaneous entropy contours at 98% span. The transient results between 6.13 rotor revolutions and 13.13 rotor revolutions are shown here. As the mass flow decreases from the design point toward the stall point, the interface between the high-entropy tip leakage vortex and the upstream flow progressively shifts forward, becoming more tangential to the main flow before ultimately turning perpendicular. At 6.13 rotor revolutions, the tip leakage vortices of the aft rotors become perpendicular to the flow, causing spillage at the leading edge of the subsequent aft blades (marked by A and B). Furthermore, TLV1 also serves as double leakage for the aft rotor of the next blade passage. Despite this, the tandem rotor remains in a stable operating regime. The local perturbation created by the higher tip gap increases with each rotor revolution. This causes spillage ahead of the leading edge of the subsequent forward rotor blade. Within one revolution (7.13 revs), forward rotor spillage can be observed, particularly affecting the four forward rotor blades. This spillage increases the local incidence near the tip of the forward rotor, resulting in localized flow separation. Small disturbances arising from the leading-edge separation coalesce, forming a rotating stall cell that grows in strength and size as it rotates in the direction opposite to rotor rotation.

Using entropy contours, Fig. 8 illustrates the transient nature of the stall cell in the full rotor domain. The postprocessing plane is drawn at the exits of both the forward and aft rotors. At 6.13 revolutions, the exits of the forward and aft rotors primarily exhibit axisymmetric flow, with most loss areas concentrated near the tip due to tip

leakage vortices. By 7.13 revolutions, the loss in the tip region begins to expand because of spillage at the leading edge of forward rotors and subsequent flow separation, disrupting the flow's symmetry. The interaction between the forward and aft rotor tip leakage vortices exacerbates the loss, which is reflected at the exit to the aft rotors. As multiple separated regions merge, they form several short-length scale disturbances. These disturbances then combine into a single stall cell, which rotates counter to the rotor's direction with approximately 0.63 times the rotor speed in the fully developed stall region. As the stall cell rotates and grows in size, it affects more and more blade passages. Within 1.5 rotor revolutions, it spans the upper half of three blade passages. By 9.13 revolutions, stall cells fully occupy three blade passages and partially affect two adjacent passages. The stall cells continue to expand as they rotate, and by 13.13 revolutions, they occupy 11 blade passages, either partially or fully. This growth may be attributed to the formation of multiple vortex structures, which necessitate further investigation.

Two key insights emerge from the results presented in Figs. 7 and 8. First, aft blade spillage first took place, which subsequently contributed to the spillage of the front blade. Second, FB LE spillage spans around 4–6 blade passages (at 7.13 revs); however, the stall cell that later develops (at 7.63 revs) is evident only in 2–4 passages, which means that all LE spillages do not result in the formation of stall cells. Previous research on conventional rotors^{17–26} has concluded that the spillage of the tip leakage vortex ahead of the rotor leading edge increases flow incidence, promoting leading-edge flow separation, which subsequently evolves into a rotating stall. In a tandem rotor configuration, the spillage of the tip leakage vortices ahead of the forward rotor leading edge plays a similar role. The multiple small disturbances combine into a single stall cell and rotate in the direction opposite to rotor rotation. The flow mechanism involved in this transition is further explained in Sec. III B 1.

1. Initiation of stall

To understand the initiation of the stall phenomenon in the complex flow field of the tandem rotor, the resolution is further increased with a small-time window. This section includes the transient results between 6.68 rotor revolutions and 7.95 rotor revolutions. Here, 6.68 rotor revolutions are marked as $t = 0$. Figure 9 shows the circumferential variation of axial velocity just ahead of the forward rotor leading edge. The turboline is drawn at 98% span. At $t = 0$, the decay in axial velocity is observed between the blade passages confined between 130° and 230° . As tip leakage strengthens, the blockage increases, and the axial velocity further reduces. Interestingly, the locus of minimum axial velocity remains relatively unchanged until the stall initiates. The reduction in axial velocity produces a cascading effect. As the axial velocity decreases, the flow incidence increases. Higher incidence promotes flow separation and increases blockage, which further reduces axial velocity and increases incidence. At $t = 12T/19$, the minimum axial velocity reduces to zero. The locus of minimum axial velocity changes after the stall inception, and it starts propagating in the circumferential direction. This low-velocity region is associated with stall cell formation. The stall cell becomes bigger and stronger as it rotates; therefore, the axial velocity drops further and further negative.

Figure 10 shows the instantaneous pressure contours at 98% span. The low-pressure regions near the leading-edge suction surface are associated with the tip leakage vortices. At $t = 0$, in a few blade

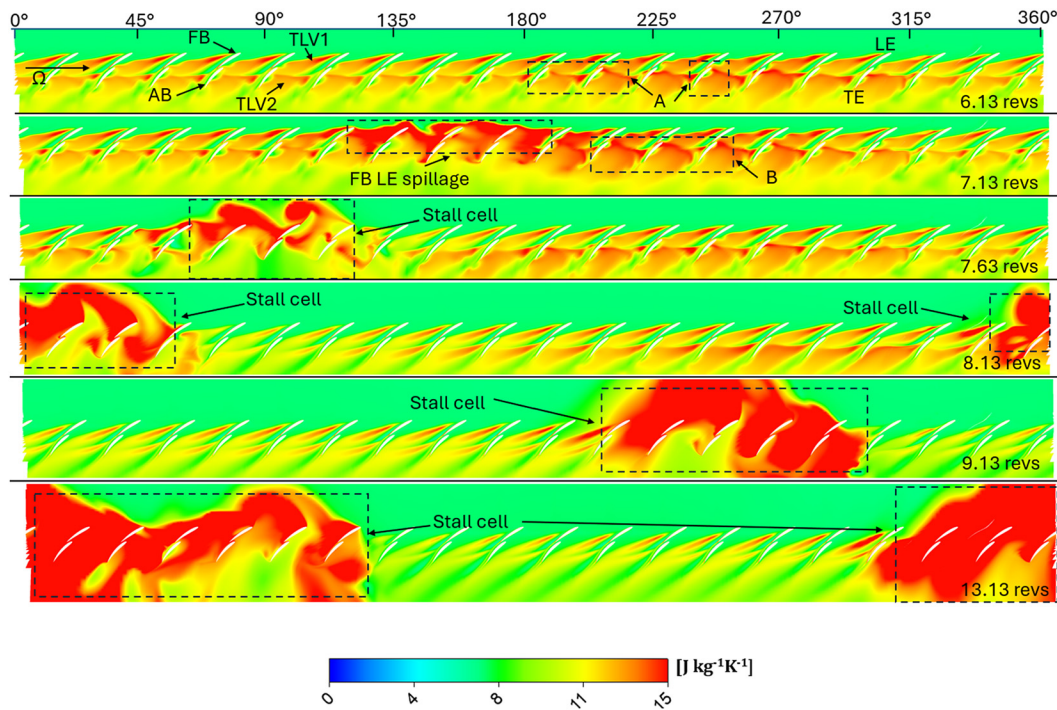


FIG. 7. Instantaneous contours of entropy at 98% span.

passages, the low-pressure region from the trailing edge of the aft rotor connects to the leading edge of the next forward rotor (marked as a black dotted elliptical shape). At the next time step, $t = 4T/19$, the low-pressure regions enlarge in each blade passage. Particularly, the low-

pressure regions experience a significant change in four blade passages, ranging from 125° to 180° . The next time step sees a further increase in the low-pressure regions for blades positioned around 135° , followed by higher pressure regions for the preceding blades.^{18,20}

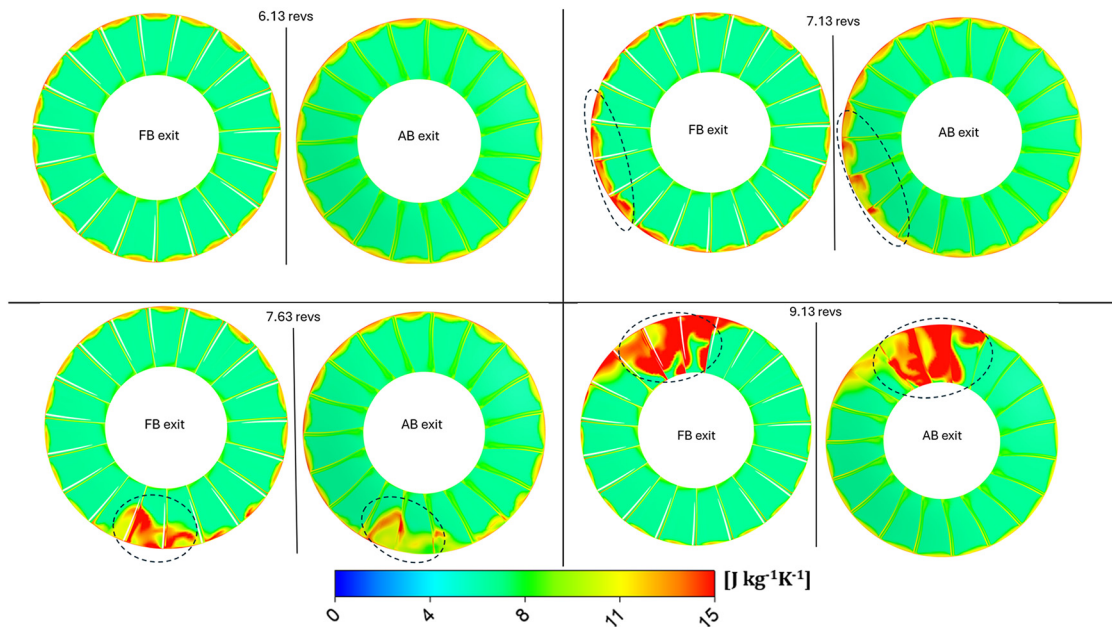


FIG. 8. Instantaneous contours of entropy at exit of forward rotor (FB exit) and aft rotor (AB exit).

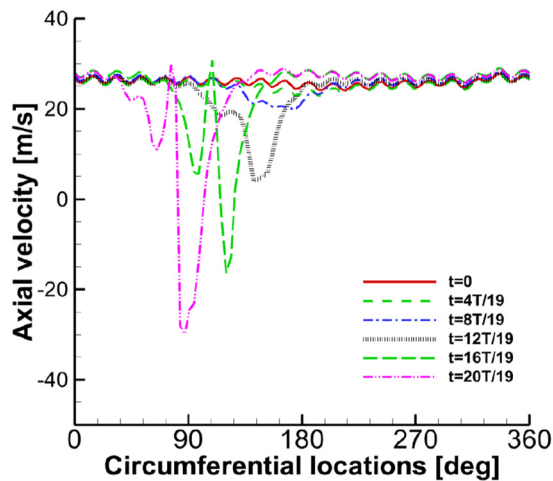


FIG. 9. Circumferential variation of axial velocity just ahead forward rotor leading edge at different time steps, turbine at 98% span (between 6.68 rotor revs and 7.95 rotor revs, 6.68 rotor revs as $t = 0$).

Multiple low-pressure regions are associated with different vortices formed due to flow separation over the blade surfaces. A discrete high-pressure spot is also observed away from the blade surface, aligned with the forward rotor leading edge. At $t = 16T/19$, the low-pressure regions become larger and change their position, moving in the opposite direction of the rotor rotation. The strongest low-pressure region near the forward rotor leading edge is linked to the casing side of the tornado vortex.²⁰ This also impacts the succeeding and preceding blades. The succeeding blade passage experiences a reduction in pressure, while the preceding blade passage experiences an increase in

pressure. The blockage created by the flow separation causes pressure to rise in preceding blade passages.

Figure 11 shows the interaction of tip leakage vortices at different time steps. Two forward and two aft rotor blades are selected to highlight the transition. Specifically, the Rainbow color map is used for the forward rotor tip leakage (TLV1), while the Divergent Cool-to-Warm color map is used for the aft rotor tip leakage (TLV2). At $t = 0$, the tip leakage of the aft rotor (TLV2) spills ahead of the leading edge of the aft rotor in the succeeding blade passage. The TLV2 changes its trajectory between the blade passages, possibly post-vortex breakdown.^{12,35–37} However, the forward rotor is still free from leading-edge spillage. At $t = 4T/19$, the aft rotor leakage vortex further changes its direction and starts spilling near the leading edge of the forward rotor. The tip leakage vortex of the forward rotor (TLV1) also changes its trajectory but still spills around 10% of the forward rotor chord. At $t = 8T/19$, both TLV1 and TLV2 continue to move further upstream, causing the leading edge of the forward rotor to be affected by the spillage from both TLV1 and TLV2. At this time step, the tip leakage vortex of the aft rotor moves in the reverse direction before it interacts with the tip leakage of the forward rotor and the main flow, moving in a line parallel to join the leading edge of the forward rotors. This shift is also evident in the tip leakage vortex of the forward rotor. At $t = 12T/19$, the forward rotor spillage becomes further intensified. At $t = 16T/19$ and $t = 20T/19$, the flow inside the tandem rotor undergoes a complete breakdown, which pushes the tip leakage vortex further upstream. Furthermore, the vortices originating from the rotor blade separation vigorously interact with these leakage vortices, causing spillage to move further upstream of the forward rotor leading edge.

Spillage is quantified using the reverse mass flow rate. The post-processing planes are positioned just ahead of the forward and aft rotor leading edge. The spillage data correspond to a single forward and aft rotor. The blade most affected by the spillage is included here. Only the area near the tip of the blade is considered for spillage analysis.

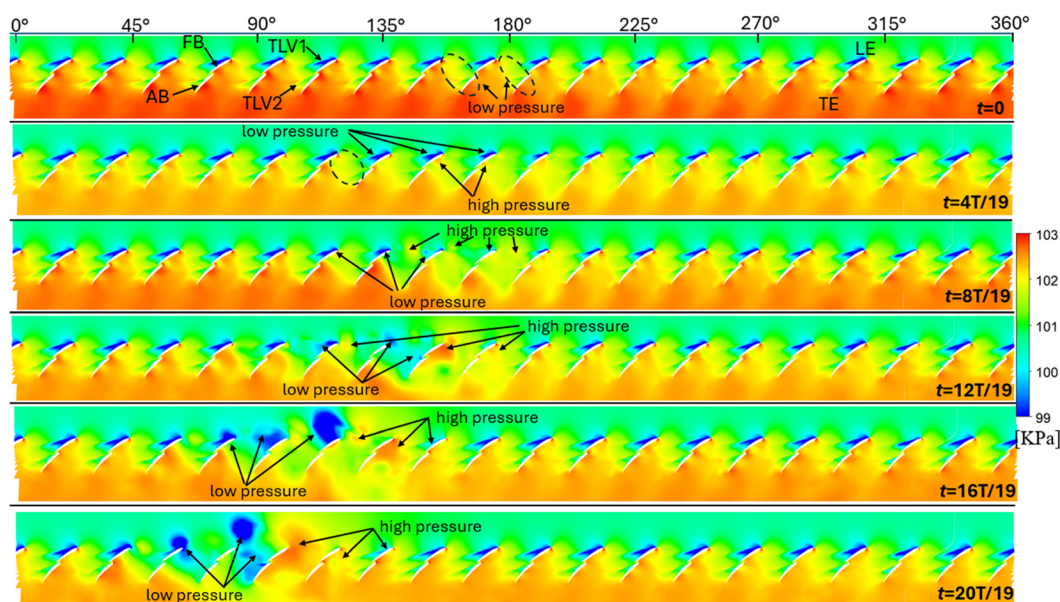


FIG. 10. Instantaneous contours of pressure at 98% span (between 6.68 rotor revs and 7.95 rotor revs, 6.68 rotor revs as $t = 0$).

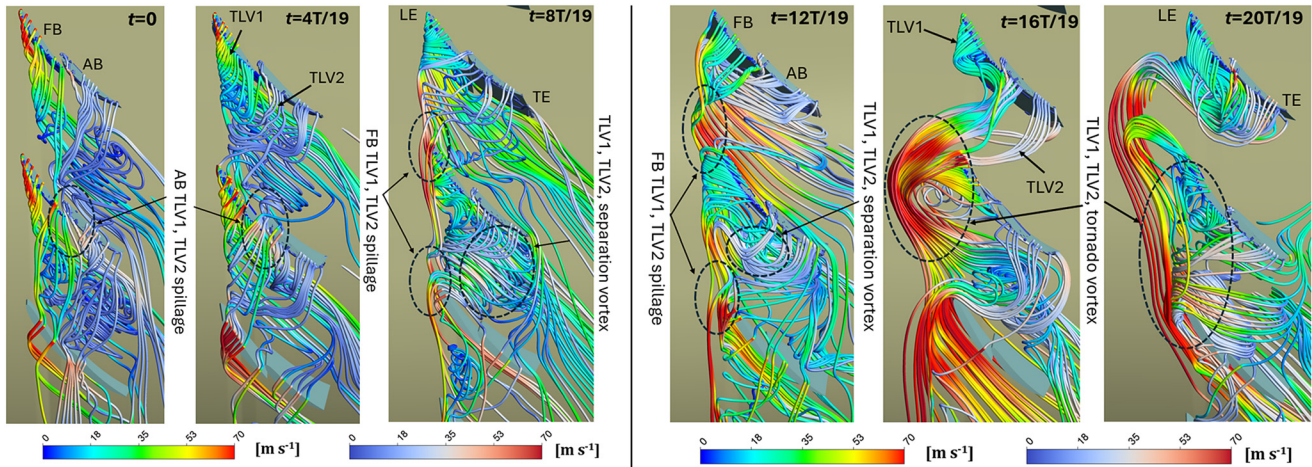


FIG. 11. Transient nature of tip leakage vortices (between 6.68 rotor revs and 7.95 rotor revs, 6.68 rotor revs as $t = 0$). Rainbow color for the forward rotor tip leakage (TLV1) and Divergent Cool-to-Warm color map for the aft rotor tip leakage (TLV2).

Additionally, 25% on either side in the circumferential direction is included to capture the correct spillage trend. For the forward rotor, the negative mass flow rate remains constant at around -0.0012 kg/s from $t = 0$ to $t = 4T/19$ as no spillage occurs until $t = 4T/19$. At $t = 0$ and $t = 4T/19$, the negative mass flow rate is solely due to boundary layer effects near the casing. At $t = 8T/19$, the reverse mass flow rate increases to -0.0029 kg/s due to spillage from TLV1 and TLV2 and further rises to -0.0235 kg/s at $t = 16T/19$ (Fig. 11). The aft rotor experiences higher spillage than the forward rotor due to the combined influence of TLV1 and TLV2, even at $t = 0$. Boundary layer effects also contribute. The AB spillage increases from -0.0015 kg/s at $t = 0$ to -0.0312 kg/s at $t = 16T/19$. In addition to TLV1 and TLV2, separation vortices from FB also contribute to the rise in reverse mass flow rate for the aft rotor at $t = 16T/19$ (Fig. 11).

2. Development of the tornado vortex

Figure 12 illustrates the instantaneous skin friction lines over the blade suction and pressure surfaces, captured at a selected time step between $t = 0$ and $t = 24T/19$. These lines are drawn over the four most affected blades, labeled 1–4, moving in the direction opposite to rotor rotation. At $t = 0$, a large radial flow is observed over the forward rotor suction surface near the hub region (RL_h). For all blades, flow separation is noticeable near the trailing edge of the aft rotor suction surface (SL_{ab}), although the radial flow is significantly lower for aft rotors. Near the tip region of forward rotors, the surface friction lines show very mild separation (SL_t), which is insignificant. In contrast, the skin friction lines near the tip region of the pressure surface exhibit significant curvature, suggesting a strong radial pressure gradient in that region (RL_t). Tip leakage vortices from the forward and aft rotor blades impinge on the pressure surface of the subsequent blades, contributing to the pressure gradient and particularly affecting blades 2, 3, and 4. This curvature is further influenced by the flow moving from the pressure side to the suction side through the tip gap. By $8T/19$, significant changes are observed near the tip regions of blades 2 and 3. Flow separation begins near 50% chord of the forward rotor suction surface of forward blade 2, occupying a 10% span from the tip. The leading-edge

separation over the forward rotor suction surface is reduced for blade 3. Interestingly, separation near the aft rotor suction surface is much lower than the forward rotor separation. Additionally, the blockage near the tip region deflects streamlines toward midspan, improving the flow and shifting the separation line (SL_{ab}) further near the trailing edge. The interaction of TLV1 and TLV2 with the pressure surface of the subsequent blades becomes more pronounced, with stronger flow separation and radial lines (RL_t) observed near the tip region. A saddle point (SP) is observed near the tip for forward rotor blades 1, 2, and 3. Additionally, a small flow separation is observed near the pressure side hub region (SL_h).

At $t = 16T/19$, the separation region over the forward rotor suction surface enlarges, occupying a significant portion of blades 1–3. The separation lines are also observed near the leading edge of the forward rotors 1–3. The skin friction lines over the suction surface for blade 1 are directed toward the blade hub. Due to higher momentum transfer toward the hub region, the radial flow and flow separation are suppressed for blades 1 and 2. The saddle points on blades 1 and 2 move further away from the tip region. A vortex center (FP) is observed around 60% span near the leading edge of the forward rotor 2. Another vortex core is observed over the forward rotor suction surface 3, around 80% span. On the other hand, the pressure sides of all blades are severely affected by the formation of various vortex structures and their interactions. For blade 2, the separation vortex's origin is approximately at 70% span, occupying a significant portion of both the forward and aft rotors. Furthermore, the vortex from suction surface blade 2 connects to the pressure surface of blade 3, resulting in a nodal point (NP) on blade 3. By $24T/19$, the vortex center shifts to midspan. Small vortices observed earlier merge to form a larger vortex that occupies the entire span of two blade passages. The suction surfaces of blades 2 and 3 are severely affected. The suction surface of the forward rotor blade 2 is completely occupied by radial flows, which are directed toward the hub. This is due to the formation of a much larger vortex near the upper span, which completely blocks the flow. As a result of this blockage, the flow is directed toward the hub region. Furthermore, Blade 3 is also completely submerged in reverse flow.

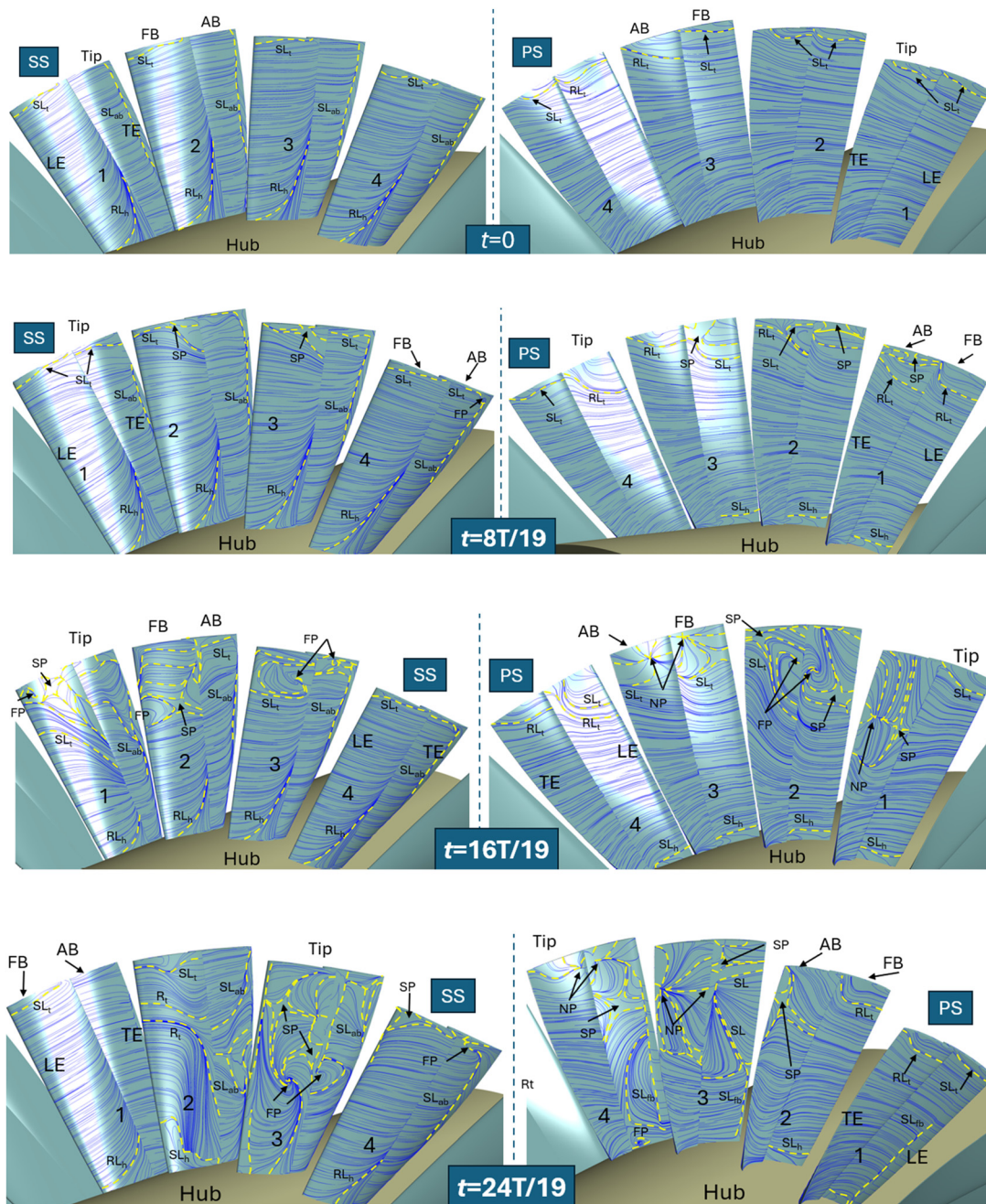


FIG. 12. Transient nature skin friction lines over blade suction surface (SS) and pressure surface (PS) (between 6.68 rotor revs and 7.95 rotor revs, 6.68 rotor revs as $t = 0$).

The core of this separation vortex is observed around 50% span of Blade 3. The formation of these vortices also disrupts and completely breaks down the flow over the pressure surface of the next blade.

Figure 13 presents the instantaneous vortex structures within the blade passages, normalized using Q criteria and colored with normalized helicity.¹² The vortex structures shown in Fig. 13 are visualized

using an iso-surface based on the Q -criterion ($Q = 2.36 \times 10^6 \text{ [s}^{-2}\text{]}$). At $t = 0$, TLV1 and TLV2 spill near 20% of the forward blade chord, generating a significant pressure gradient in the radial direction. Vortex breakdown^{12,35–37} is observed for both TLV1 and TLV2 across all four blade passages. By $8T/19$, TLV1 and TLV2 begin spilling ahead of the leading edge of the forward rotor, increasing the incidence near

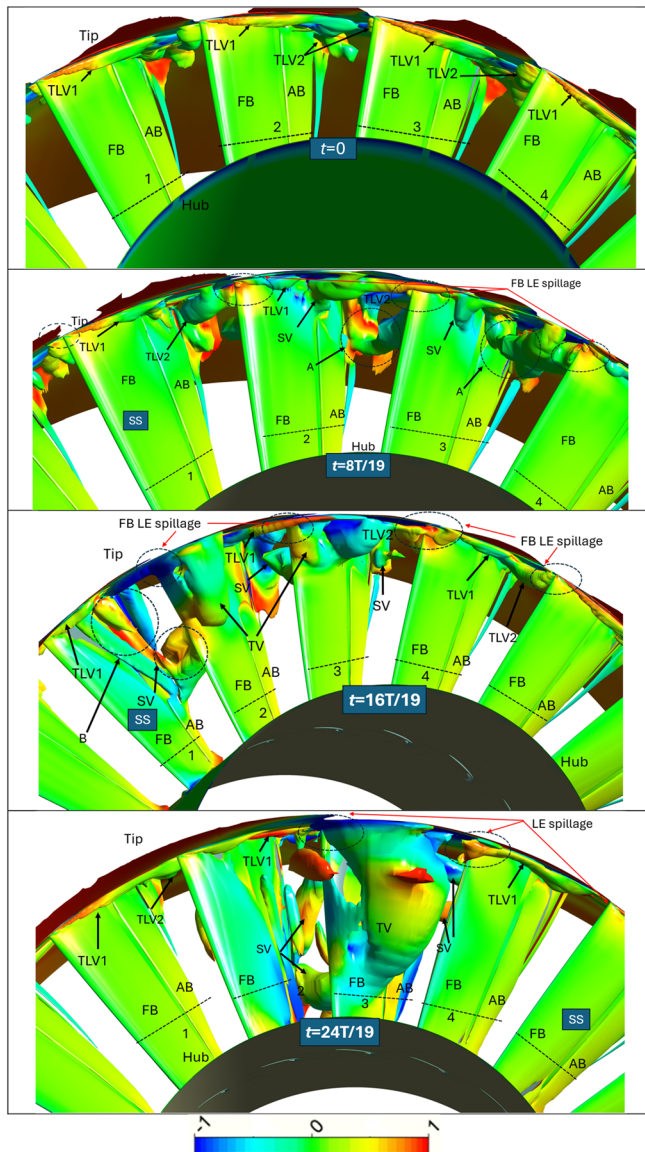


FIG. 13. Transient nature of vortex structures (between 6.68 rotor revs and 7.95 rotor revs, 6.68 rotor revs as $t=0$). The iso-surface of the Q -criteria ($Q = 2.36 \times 10^6 \text{ [s}^{-2}\text{)]}$ is shown, with vortices colored based on normalized helicity.

the tip region and resulting in a separation vortex (SV) on blades 2 and 3.^{18,19,22} The strength of the SV over the forward blade 2 is higher than that over the forward blade 3, with these vortices forming between 60% of the chord and the trailing edge of the forward rotor. Furthermore, TLV1 and TLV2 merge with these separation vortices, convecting toward the pressure surface of the subsequent blades, marked as region A. This interaction results in a large region of separated flow and radial flow on the pressure surface of blades 3 and 4 near the tip area ($t = 8T/19$ of Fig. 12).

At $16T/19$, several vortex structures are evident inside the blade passages. For blade 1, a separation vortex is observed at the trailing

edge of both the forward and aft rotors (marked as B). Furthermore, the leading-edge separation vortex (SV for blades 2 and 3 at $8T/19$) of the forward rotor evolves into a stronger and bigger tornado vortex (TV).^{18–20} The suction leg of TV is observed near the leading edge of the forward rotor, around 60% span, while its casing leg shifts upstream and is connected to the casing. Additionally, the separation vortex near the forward and aft trailing edges (SV) becomes more pronounced. These vortices travel toward the pressure surface of the subsequent blades, creating various vortex structures.

By $24T/19$, many of these vortices merge to form a much stronger tornado vortex (TV) that spans the entire blade length. The suction leg of the tornado vortex moves toward the lower span and is located over the forward rotor suction surface at approximately 30% of the blade span. Its other end connects to the casing upstream of the forward rotor, encompassing the entire blade passage. Vortex structures originating from the suction surfaces of blades 2 and 3 vigorously interact with the pressure surface of the next blades. Other vortex structures from the aft rotors, apart from TLV2, appear to be intermittent; some of these structures collapse, with new vortices subsequently arising (SV). As the tornado vortex grows larger, its casing end moves closer to the leading edge of the next forward rotor. The blockage effect also pulls TLV1 and TLV2 further ahead of the rotor. Cumulatively, these vortices increase the incidence angle on the succeeding forward rotor, leading to leading-edge flow separation and the formation of new vortices. These separation vortices then interact with the next blade, causing the leading-edge separation to propagate. This process continues, eventually driving the tandem rotor into stall.

3. Transient nature of the gap nozzle flow and blade loading

The tandem blade configuration is characterized by the nozzle gap effect. The transient nature of gap nozzle flow is shown by velocity contours. Figure 14 shows the velocity contours at 98% span. The four blade passages, which are at the center of the stall transition, are shown here. The momentum transfer through the gap-nozzle mostly affects the efficiency of the tandem configuration. The higher momentum transfer through the gap nozzle suppresses the flow separation over

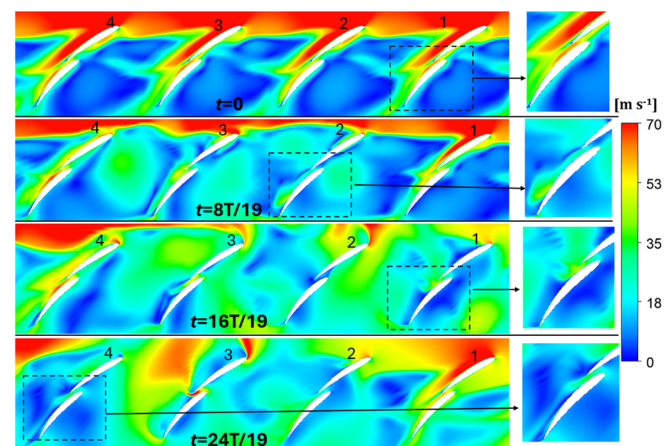


FIG. 14. Instantaneous flow inside gap nozzle, velocity contours at 98% span location, (between 6.68 rotor revs and 7.95 rotor revs, 6.68 rotor revs as $t=0$).

the aft blade suction surface. At $t = 0$, sufficient momentum transfer ensures attached flow over all four aft rotors. At $t = 8T/19$, the momentum transfer through the nozzle gap is significantly affected due to forward rotor spillage and subsequent flow separation over the forward rotors. Following that, an imminent flow separation is visible over the aft rotor suction surface. All four aft rotors exhibit a decay in the nozzle-gap effect, with blades 2 and 3 displaying a more prominent effect. At $t = 16T/19$ and $t = 24T/19$, the formation of a tornado vortex and other vortices further weakened the flow through the gap nozzle, leading to significant flow separation over the aft blade suction surface.

Figure 15 illustrates instantaneous blade loading at 98% span for four blades, which are at the center of the stall transition and where most changes in blade loading are observed. At $t = 0$, the maximum loading point of all four forward rotors is near the leading edge. The pressure profile over the suction surface remains unchanged for both the forward and aft rotors. However, the loading pattern, particularly over the pressure surface, demonstrates the transient nature of the flow. The tip leakage vortices (TLV) of preceding blades impinge on the pressure surface of subsequent blades (Figs. 12 and 13). The blockage of TLV1 and TLV2 creates an additional pressure rise (forward rotors 2 and 4). These vortices significantly reduce the blade loading of

the aft rotors. At $t = 8T/19$, both forward and aft rotors experience a drastic change in the loading pattern. The spillage of TLV1 and TLV2 attenuates the blade loading of forward rotors 2, 3, and 4, significantly affecting the loading near the leading edge. The pressure surface of the forward rotor 2 experiences another dip around 70% of the forward rotor chord. The flow separation over the forward and aft rotor suction surfaces further reduces diffusion characteristics. The ineffectiveness of the gap nozzle leads to a reduction in blade loading for aft rotors 2 and 3, though the loading of the aft rotor blade 4 improves (Fig. 14). At $t = 16T/19$, the formation of different separation vortices on the suction and pressure surfaces alters the blade loading of both rotors. Flow separation over both pressure and suction surfaces limits the diffusion characteristics of aft rotor 1. Forward rotors 2, 3, and 4 experience leading-edge separation, reducing loading near the leading edge. Once the flow reattaches over the suction surface, the diffusion capability of the forward rotor 2 improves. The formation of tornado vortices and other vortex structures within blade passages 2 and 3 causes a significant pressure drop near the trailing edge of the forward blade. The leading edge of the aft rotor 3 also experiences a substantial pressure drop due to the influence of a tornado vortex. At $t = 24T/19$, forward and aft rotors 2, 3, and 4 are primarily affected by the tornado vortex

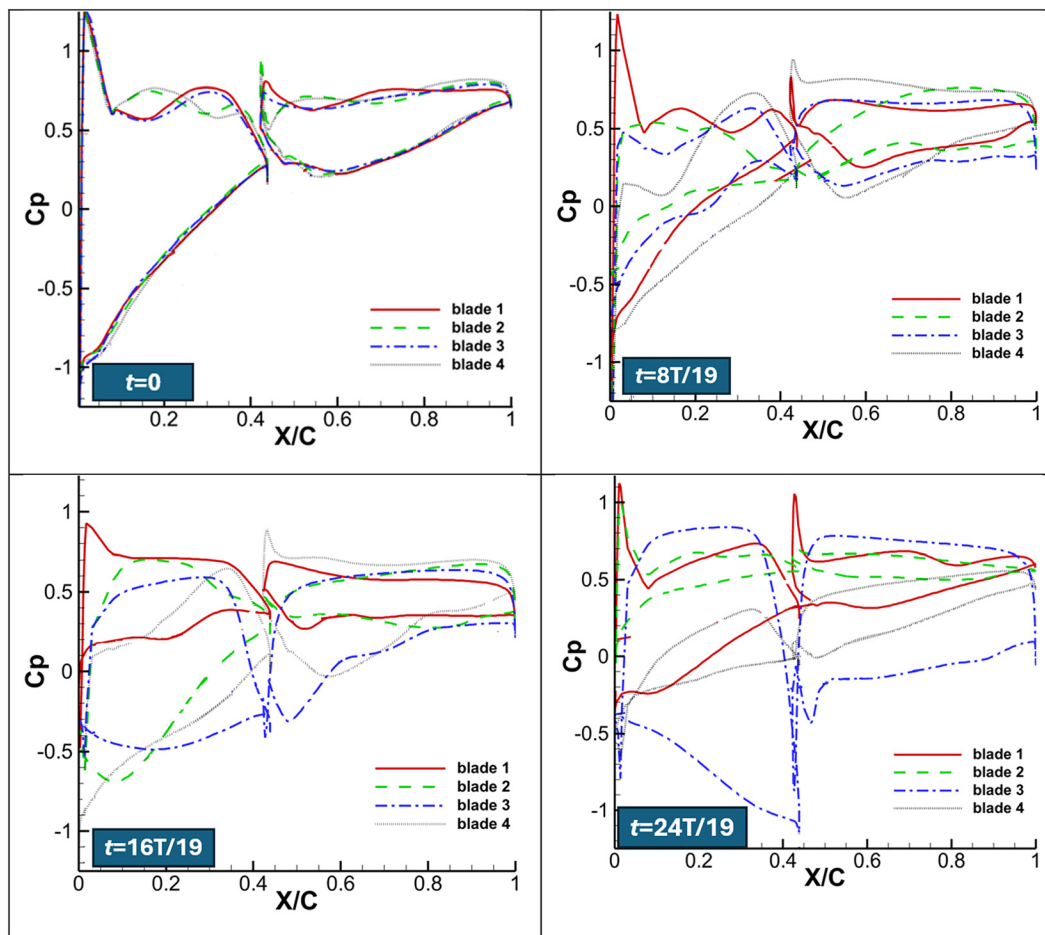


FIG. 15. Instantaneous blade loading at 98% span (between 6.68 rotor revs and 7.95 rotor revs, 6.68 rotor revs as $t = 0$).

and other vortices, while forward and aft rotor 1 has partially recovered. Blade 2 remains stalled. The influence of the tornado vortex causes an exceptionally high blade loading for blade 3. The casing end of the tornado vortex generates a large low-pressure region on the suction surface, while the blockage effect from this vortex increases the pressure in the preceding passage, resulting in a monumental rise in blade loading. Particularly, the trailing edge of the forward rotor becomes heavily loaded (Figs. 10 and 13).

C. Unsteady analysis of pressure data

This section discusses the analysis of the unsteady pressure data collected from 1000 monitoring points. Data for pressure and absolute velocity are recorded at 1000 monitoring points near the casing, uniformly distributed across ten axial locations (−10%C, 0%C, 14%C, 28%C, 42%C, 56%C, 72%C, 88%C, 100%C, 108%C) and circumferentially around the rotor casing. Each monitoring point collects data at a sampling frequency of 17 097 Hz, which is calculated based on the time step used in the simulation. The transient simulation is run for a period of 0.297 s, which corresponds to 13.38 rotor revolutions, yielding 5083 data recordings per monitor point. The unsteady pressure data are analyzed using Fourier Transform Analysis, Filtered Signal Analysis, and a Feature Algorithm. A brief description of these analysis methods is provided in Subsection III C 1.

1. Methodology

a. Fourier transform analysis. The initial step involves calculating the Fourier transform of the 5083-point pressure time series at each monitoring point. To facilitate the comparison of Fourier amplitudes across axial positions, the maximum and minimum amplitude ranges are standardized for all plots. Only positive frequencies below 1000 Hz are plotted. This allowed for the identification of the frequency range associated with the stall cells.

b. Filtered signal analysis. To examine the temporal and spatial characteristics of the pressure disturbance, the pressure data within the identified frequency range are filtered using a 4th order Butterworth bandpass filter. The filtered pressure trace is plotted over time for various angular and axial locations. A frequency vs amplitude plot for the filtered signal is also generated to further understand the disturbance characteristics. It is noted that the disturbance amplitude for stall cells decreases and becomes less discernible at downstream axial locations due to other disturbances of similar small amplitude.

c. Pressure disturbance detection: Feature algorithm. An algorithm is developed to enhance the detection of pressure disturbances circumferentially and axially, even with temporal shifts. The process begins by dividing the unfiltered pressure trace into windows sized by the inverse of the minimum filter frequency ($1/f_{\min}$) and a sliding size of the inverse of the maximum filter frequency ($1/f_{\max}$). This windowing ensures the capture of the largest and smallest pressure fluctuation cycles within each window,

$$W_{\text{slide}} = \frac{1}{f_{\max}}, \quad (1)$$

$$W_{\text{size}} = \frac{1}{f_{\min}}, \quad (2)$$

$$W_{\text{slide}} = \left[P(t_i), P\left(t_i + \frac{1}{f_{\min}}\right) \right], \quad (3)$$

$$t_{\text{avg}}^{W_i} = \text{mean}\left(t_i, t_i + \frac{1}{f_{\min}}\right). \quad (4)$$

The parameters associated with a window W_i are defined in Eqs. (1)–(4). t_i is the starting time step of the window, W_i .

Starting at the 0° angular position of the first axial location, the Fourier transform of the first window $F\{W_i\}[k]$ is computed. This initial window's amplitude is stored as a feature vector A_0 for category 1 (the term category is simply a label given to the feature vector). Subsequent windows at the same axial location undergo a Fourier transform $F\{W_i\}[k]$, and the Euclidean distance d_{features}^i between their amplitudes and the stored feature vectors A_j is calculated. If this distance exceeds a threshold, the new window is assigned to a new category, and its amplitude is stored as a new feature vector. If the distance is below the threshold, the window is assigned to the existing category, and its feature vector is updated,

$$F\{W_i\}[k] = \sum_{n=0}^{N-1} P(t_i + n\Delta t) \cdot e^{-j(2\pi/N)kn}, \quad (5)$$

$$d_{\text{features}}^i = \sqrt{\sum_k \left(F\{W_i\}[k] - A_j^k \right)^2}. \quad (6)$$

In above equations, k is the k th Fourier frequency and N is the number of points in window W_i .

This process iterates through all windows at each axial and angular location, generating new features or updating existing ones based on the Euclidean distance threshold. When multiple features meet the threshold criterion, the feature closely matching the current window is selected, and its vector is updated with the new window's amplitudes. The flow chart for the complete algorithm is given in Fig. 16.

The proposed algorithm effectively identifies similar pressure disturbances across the circumference, time, and axial locations, even as these disturbances diminish into low-amplitude variations at downstream axial positions, albeit with reduced temporal resolution. By replacing the Fourier amplitudes of the most recent representative window for each category with a feature vector, the algorithm ensures the creation of a new category whenever the current features significantly deviate from the window's characteristics. Notably, this approach facilitates near real-time identification of similar features without requiring prior knowledge of future pressure traces.

2. Results of unsteady analysis of pressure data

Although the pressure data are recorded at ten axial points, only the pressure data for three axial locations, −10%C, 0%C, and 14%C, are analyzed. At higher chord locations, the strength of the pressure signal fades, making it difficult to separate low amplitude disturbances from the stall cell signal. The Fourier transform is applied to pressure traces at axial locations −10%C, 0%C, and 14%C. Figure 17 shows the Fourier transform based on pressure data. All significant amplitudes are found below 200 Hz at all axial locations. For downstream chord location, the Fourier amplitude is reduced in magnitude for all frequencies below 200 Hz.

The pressure data are further filtered within the frequency range, $f_{\min} = 50$ Hz and $f_{\max} = 100$ Hz, to identify the origin and propagation

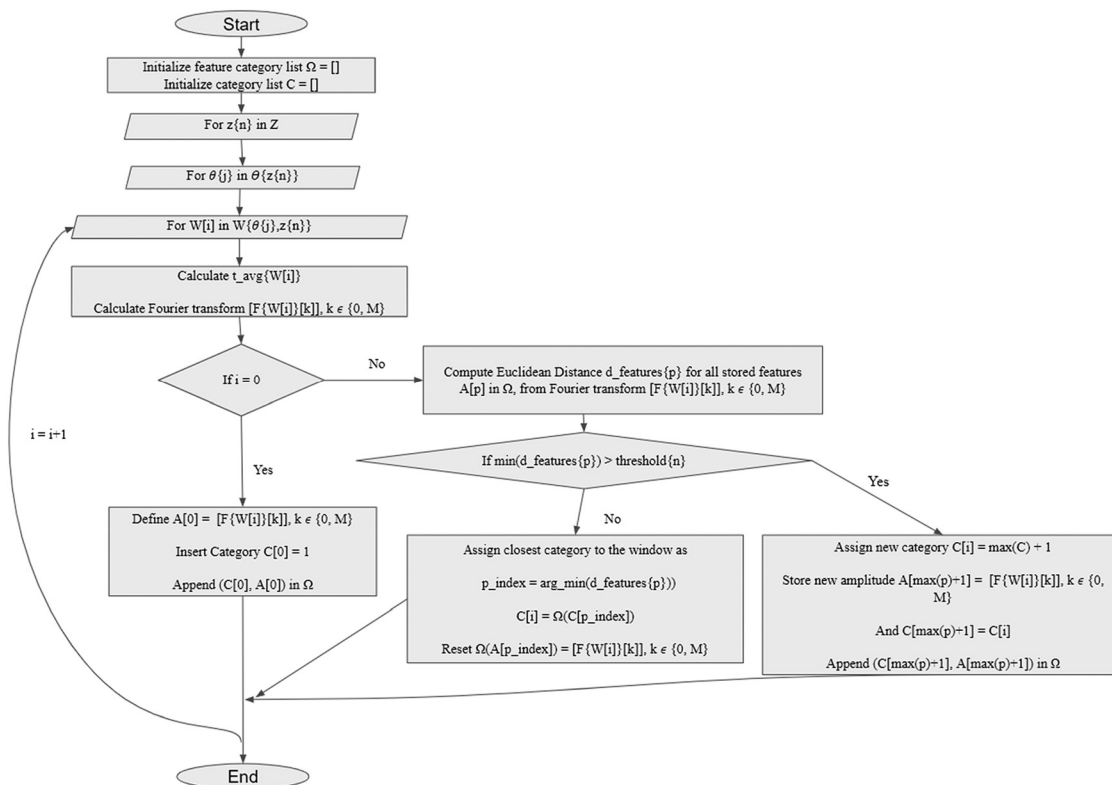
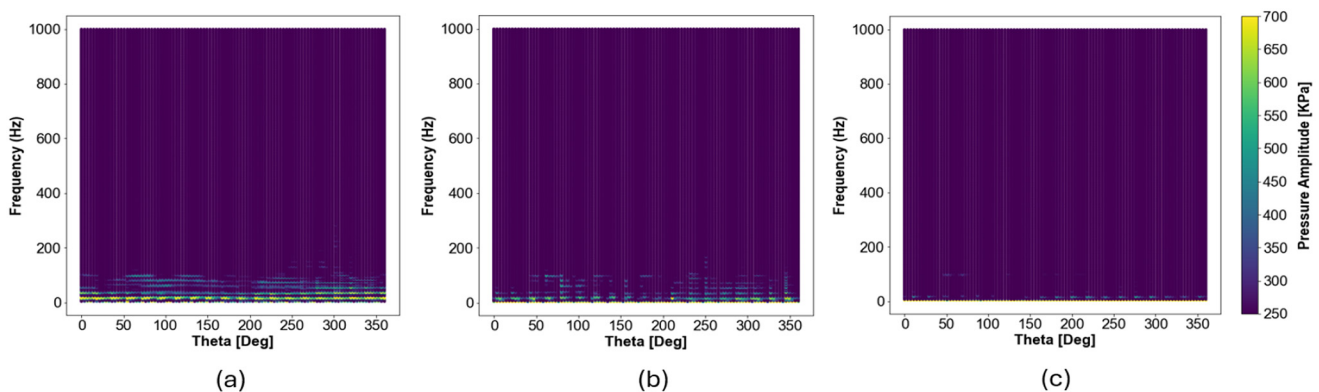


FIG. 16. Flowchart of the algorithm used for the unsteady pressure trace analysis.

of the stall cell. This range represents the lowest frequencies at which stall cells are discernible in the filtered pressure traces. Figure 18 presents the normalized pressure trace (min to max pressure) over time (rotor revolutions) and angular position for three axial locations. The stall cell is observed to originate around 180° at approximately 7 rotor revolutions and persists throughout the simulation. While downstream axial locations exhibit similar behavior, the pressure amplitude diminishes significantly, causing the signal to blend with other low-

amplitude disturbances, resulting in distortion. The stall cell rotates counter to the rotor direction at approximately 0.63 times the rotor speed. Notably, small-amplitude disturbances moving at the same speed and in the same direction as the stall cell are detected at all three axial locations even before the stall cell forms.

Figure 19 illustrates the evolution of filtered pressure traces across angular positions at different axial locations. The plot includes data from 20 monitor points spanning the full annulus, with an angular

FIG. 17. Scatter plot frequency with circumferential position of pressure traces at three different axial locations, (a) $-10\%C$, (b) $0\%C$, (c) $14\%C$.

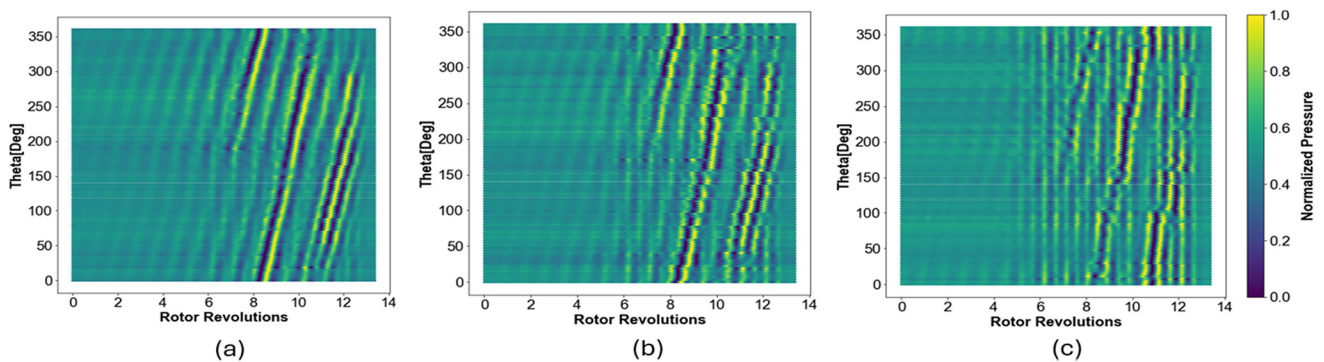


FIG. 18. Min to max normalized pressure trace across time and angular position at three different axial locations, with pressure data at each monitor point filtered between 50 and 100 Hz, (a) $-10\%C$, (b) $0\%C$, (c) $14\%C$.

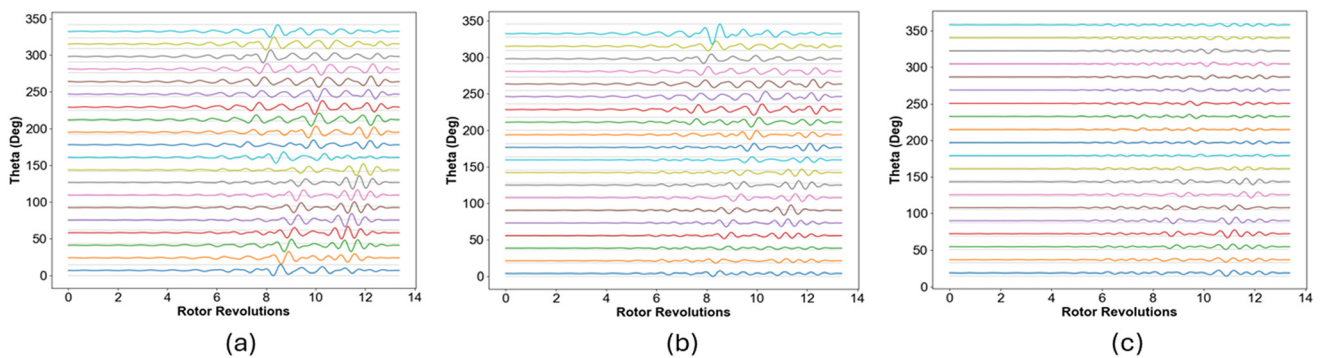


FIG. 19. Pressure traces bandpass filtered between 50 and 100 Hz for three different axial locations, and angular positions in multiple of 18° , (a) $-10\%C$, (b) $0\%C$, (c) $14\%C$.

separation of 18° between adjacent points. The 10th numerical probe, located at 180° , is the first to capture changes in the pressure trace. As the stall cell progresses, it strengthens, leading to an increase in pressure amplitude. While the stall cell's effects are also observed at the third axial location, the amplitude diminishes significantly. At downstream axial locations, the magnitudes of low-amplitude disturbances approach those of the stall cell, making it challenging to distinguish the stall cell from background disturbances.

Figure 20 presents the Fourier amplitude as a function of frequency across the full annulus. The plot indicates that the disturbance frequency is distributed over multiple frequencies rather than being confined to a single dominant frequency. This distribution of amplitude remains relatively uniform across all axial locations, with no particular bias toward any specific frequency.

Previous analysis, Figs. 17–20, relied on the availability of complete pressure data for each monitoring point. A feature-tracking

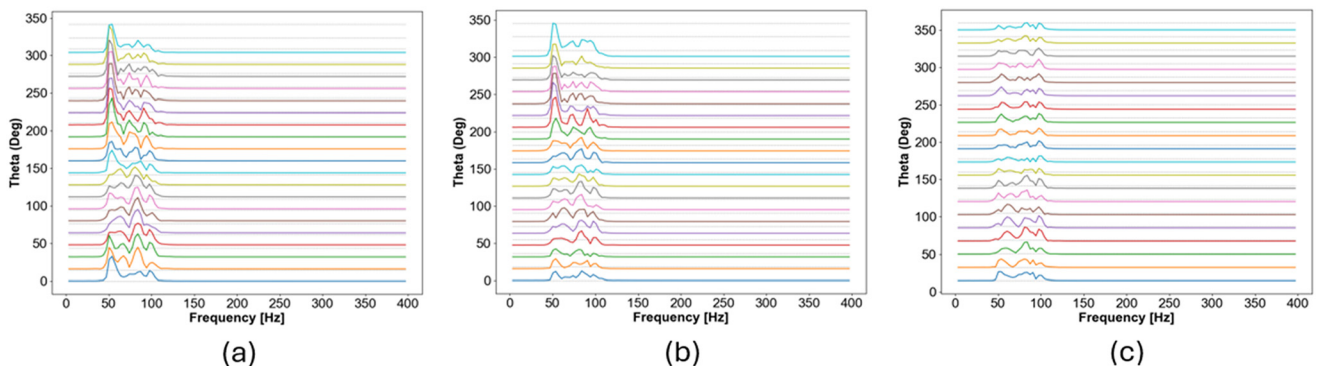


FIG. 20. Fourier amplitudes vs frequency plots for different axial and angular locations for the pressure signal filtered between 50 and 100 Hz, (a) $-10\%C$, (b) $0\%C$, (c) $14\%C$.

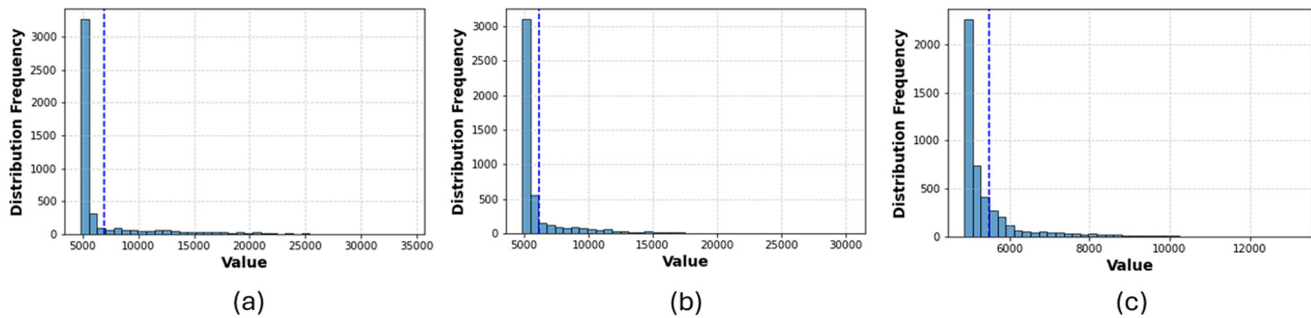


FIG. 21. Distribution of window distances and calculations of threshold value to distinguish windows for three axial locations (a) $-10\%C$, (b) $0\%C$, (c) $14\%C$.

algorithm (Subsection III C 1 c) based on Fourier amplitude distance is applied to identify similar pressure disturbances over rotor revolutions, axial location, and angular location. To identify disturbances at downstream axial locations and filter out noise, it is assumed that the frequency and amplitude characteristics of a given disturbance remain consistent across different axial and angular locations. The method to calculate the threshold distance between the windows, in order to distinguish them, was to generate a histogram of the distribution frequency of distances between windows for three axial locations. The threshold amplitude for an axial location was calculated as the distribution frequency-weighted average of the amplitudes. The threshold amplitudes for $-10\%C$, $0\%C$, and $14\%C$ locations are 6868, 6178, and 5485, respectively, as shown in Fig. 21.

Figure 22 illustrates the angular and temporal position of the feature variation for different axial locations. The algorithm successfully identified the same stall cell characteristics across different axial locations by assigning them the same category. However, it is less effective at distinguishing the pressure disturbance from low-amplitude disturbances at downstream chord locations, resulting in a distorted and thickened stall cell pressure trace.

D. Comparison of stall inception in conventional and tandem rotor

In this section, the stall inception mechanism of the tandem rotor is compared with that of a conventional rotor, highlighting both

similarities and differences. Figure 23 schematically illustrates the stall inception mechanisms for the tandem and conventional rotors. The stall inception of conventional rotors is well-documented, with numerous studies addressing it through experimental and numerical investigations.^{17–30} For conventional rotors, stall inception occurs through either long-length scale disturbances, known as modal stall, or short-length scale disturbances, referred to as spike stall. Modal stall is a progressive phenomenon, whereas spike stall is abrupt, occurring without prior warning.^{27,28} Spike stall is a localized flow phenomenon, typically confined to the rotor tip region, where it evolves into stall cells that rotate circumferentially. These stall cells disrupt the flow symmetry and are characterized by their rapid growth in size. In tandem rotors, stall cells are similarly confined near the tip region. Furthermore, these disturbances also exhibit rapid growth in both radial and circumferential directions. This suggests that the tandem rotor might follow the spike-type stall inception.

Later, Vo *et al.*¹⁹ proposed another hypothesis for spike-type stall inception in conventional rotors. It identifies two critical criteria: the spillage of tip leakage flow in front of the leading edge of the next blade and the backflow near the trailing edge. In conventional rotors, the spillage of tip leakage vortices increases the local incidence near the tip, causing leading-edge flow separation, which ultimately evolves into the rotating stall. For tandem rotors, two tip leakage vortices—TLV1 and TLV2—are present. Interestingly, spillage first occurs in the aft rotor, influenced by both forward and aft leakage vortices. Despite this, the tandem rotor remains stable, as the gap-nozzle flow effectively

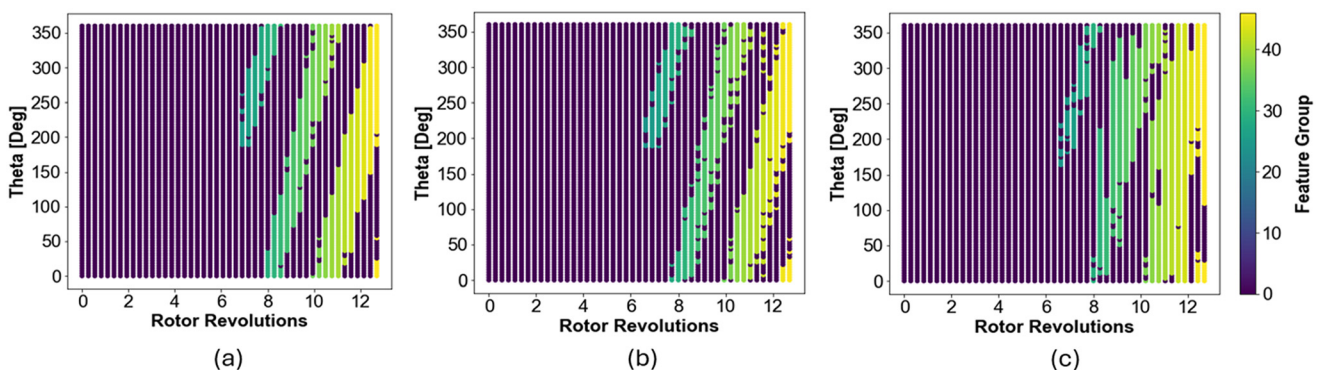


FIG. 22. Plot of features vs angular position vs rotor revolutions at three different axial locations, (a) $-10\%C$, (b) $0\%C$, (c) $14\%C$. Same feature group across different axial locations is color coded similarly.

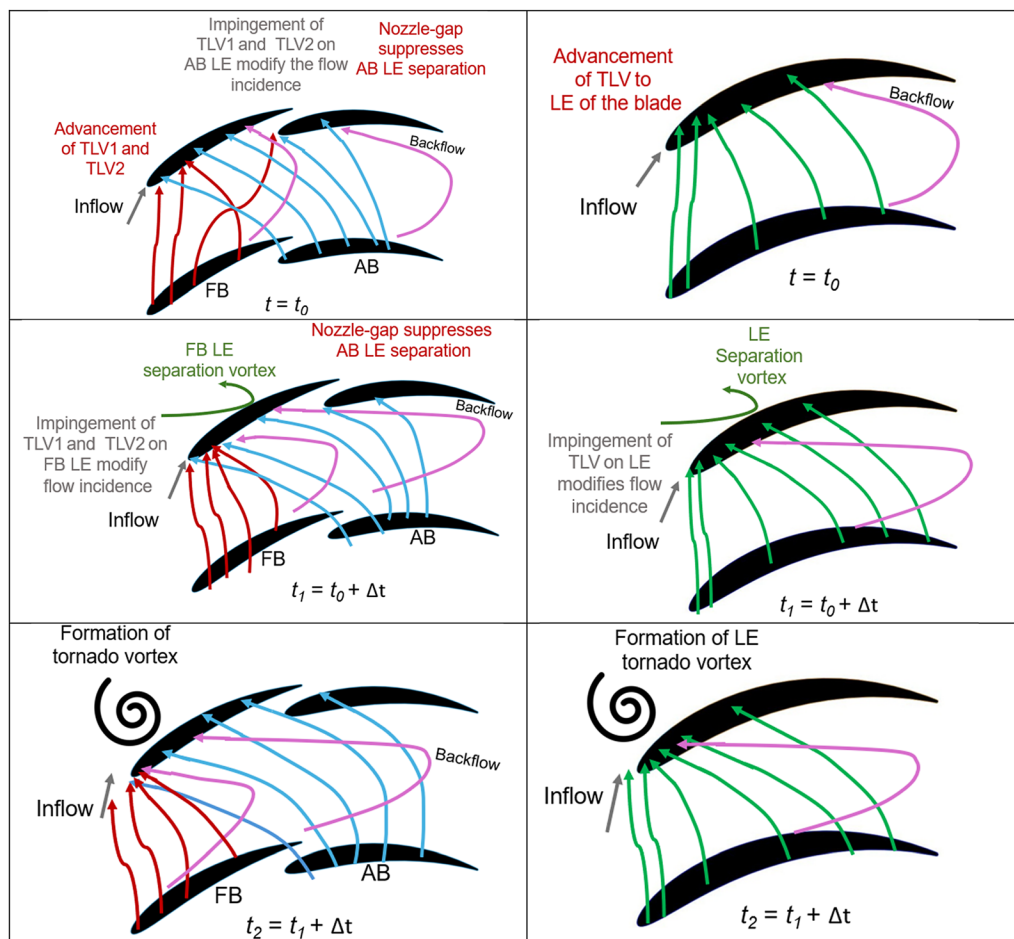


FIG. 23. Stall inception enroute in conventional rotor and tandem rotor.

suppresses any tendency for leading-edge separation in the aft rotor. However, the spillage of tip leakage vortices near the leading edge of forward rotor plays a critical role. This reduces the amount of incoming flow, increasing the local incidence beyond the critical threshold. This leads to forward rotor leading-edge flow separation, which subsequently evolves into the rotating stall. Therefore, despite having two rotors, the tandem rotor also follows the conventional spike-type stall inception mechanism commonly observed in axial flow compressors. This behavior could be design-specific, and further unsteady experimental and numerical investigations on other tandem rotor designs are necessary to reinforce this hypothesis.

Moreover, this study further corroborates previous findings regarding the performance and stability of tandem rotors, which suggest that tandem rotors are particularly sensitive to forward rotor performance. It highlights that forward rotor spillage is crucial to the tandem rotor's operation and stability and can, therefore, be considered analogous to the spillage mechanism in conventional rotors. Any active or passive stall control mechanism for tandem rotors should prioritize addressing forward rotor spillage to ensure stable operation. Importantly, many passive control mechanisms, such as axial or

circumferential casing treatments and blade tip design modifications, should primarily target the forward rotor to delay stall. Additionally, a stall warning system could be designed to monitor forward rotor spillage and trigger when forward tip spillage occurs.

IV. CONCLUSIONS

The present paper discusses a full annulus transient analysis of a highly loaded tandem rotor. The study aims to understand the stall inception mechanism of the tandem rotor and identify the role of forward and aft tip leakage vortices in stall inception. This analysis provides detailed insights into the unsteady interactions between the forward and aft tip leakage vortices, as well as other vortex structures, and their impact on tandem rotor performance. The key findings are as follows:

1. The aft rotor spillage first took place, which subsequently contributed to the spillage of the front blade. Even though the aft rotor encounters tip vortex spillage from the forward and the aft rotor of the subsequent passage, the nozzle gap effect effectively mitigates flow separation, ensuring stable operation of the tandem rotor system.

2. The forward rotor spillage is critical for the tandem rotor. This spillage increases the local incidence near the tip of the forward rotor, resulting in localized flow separation. Small disturbances arising from the leading-edge separation coalesce, forming a rotating stall cell that grows in strength and size as it rotates in the direction opposite to rotor rotation at approximately 0.63 times the rotor speed.
3. The leading-edge separation over the forward blade suction surface evolves into a fully grown tornado vortex within 16T/19 of a time period, corresponding to approximately 0.84 revolutions. The tornado vortex suction leg is located on the forward rotor suction surface, while its other end connects to the casing upstream of the forward rotor. Other vortex structures from the aft rotors, except aft rotor tip leakage vortex, are intermittent, collapsing, and reforming.
4. The formation of a tornado vortex and other vortices significantly affects the momentum transfer through the nozzle gap, leading to visible flow separation over the aft rotor suction surface. Additionally, the tornado vortex and leading-edge separation severely attenuate the blade loading of the forward and aft rotor blades.
5. All the significant disturbances are observed below 200 Hz at all axial locations. The frequency of disturbance cannot be attributed to any one frequency and is distributed over multiple frequencies.

AUTHOR DECLARATIONS

Conflict of Interest

The authors have no conflicts to disclose.

Author Contributions

Amit Kumar: Conceptualization (equal); Investigation (equal); Methodology (equal); Validation (equal); Visualization (equal); Writing – original draft (equal). **Akshay Kumar:** Conceptualization (equal); Investigation (equal); Methodology (equal); Writing – original draft (equal). **Hitesh Chhugani:** Conceptualization (equal); Investigation (equal); Methodology (equal). **Manas Payyappalli:** Conceptualization (equal); Methodology (equal); Visualization (equal); Writing – review & editing (equal). **A. M. Pradeep:** Conceptualization (equal); Methodology (equal); Supervision (lead); Writing – review & editing (lead).

DATA AVAILABILITY

The data that support the findings of this study are available from the corresponding author upon reasonable request.

NOMENCLATURE

AB	Aft blade
AO	Axial overlap = $\frac{\Delta A}{A}$
BPF	Blade passing frequency
FB	Forward rotor
C	Combined chord of tandem rotor (m)
C _p	Static pressure coefficient = $\frac{p-p_1}{0.5\rho U_t^2}$
DF	Diffusion factor

LE	Leading edge
m_d	Design mass flow rate (kg/s)
m_s	Stall mass flow rate (kg/s)
P	Static pressure (Pa)
P_0	Total pressure (Pa)
P_{01}	Total pressure at the forward rotor inlet (Pa)
P_{02}	Total pressure at the aft rotor exit (Pa)
P_1	Static pressure at the forward rotor inlet (Pa)
PP	Percentage pitch = $\frac{D_2}{D_1}$
PS	Pressure surface
RANS	Reynolds averaged Navier–Stokes
SS	Suction surface
SM	Stall margin = $\frac{m_d - m_s}{m_d}$
T	Time period
TE	Trailing edge
TLV	Tip leakage vortex
TLV1	Tip leakage vortex of forward rotor
TLV2	Tip leakage vortex of aft rotor
TV	Tornado vortex
t	time (s)
URANS	Unsteady Reynolds averaged Navier–Stokes
U_m	Peripheral velocity at mean radius (m/s)
V_x	Axial component of absolute velocity (m/s)
X/C	Percentage of chord
γ	Stagger angle (°)
θ	Camber (°)
ρ	Air density (kg/m ³)
ψ	Total pressure rise coefficient = $\frac{P_{02} - P_{01}}{0.5\rho U_m^2}$
ϕ	Flow coefficient = $\frac{V_x}{U_m}$

REFERENCES

- ¹J. A. Brent, “Single-stage experimental evaluation of tandem-airfoil rotor and stator blading for compressors, Part 2: Data and performance for stage A,” NASA-CR-120804 (NASA, 1972).
- ²K. Bammert and R. Staude, “Optimization for rotor blades of tandem design for axial flow compressors,” *ASME J. Eng. Gas Turbines Power* **102**(2), 369–375 (1980).
- ³U. K. Saha and B. Roy, “Experimental investigations on tandem compressor cascade performance at low speeds,” *Exp. Therm. Fluid Sci.* **14**(3), 263–276 (1997).
- ⁴J. McGlumphy, W. Ng, S. R. Wellborn, and S. Kempf, “Numerical investigation of tandem airfoils for subsonic axial-flow compressor blades,” *ASME J. Turbomach.* **131**(2), 021018 (2009).
- ⁵G. A. C. Falla, “Numerical investigation of the flow in tandem compressor cascades,” M.S. thesis (Institute of Thermal Power Plants, Vienna University of Technology, Austria, 2004).
- ⁶A. Kumar and A. M. Pradeep, “Design methodology of a highly loaded tandem rotor and its performance analysis under clean and distorted inflows,” *Proc. Inst. Mech. Eng., Part C* **235**(23), 6798–6821 (2021).
- ⁷L. Müller, D. Kožulović, D. Wulff, S. Fischer, and U. Stark, “High turning compressor tandem cascade for high subsonic flows—Part 2: Numerical and experimental investigations,” in *47th AIAA/ASME/SAE/ASEE Joint Propulsion Conference & Exhibit*, AIAA Paper No. 2011-5602 (AIAA, 2012).
- ⁸M. Böhle and T. Frey, “Numerical and experimental investigations of the three-dimensional-flow structure of tandem cascades in the sidewall region,” *ASME J. Fluids Eng.* **136**(7), 071102 (2014).
- ⁹Z. Song and B. Liu, “Optimization design for tandem cascades of compressors based on adaptive particle swarm optimization,” *Eng. Appl. Comput. Fluid Mech.* **12**(1), 535–552 (2018).

- ¹⁰J. Eckel and V. Gümmer, "Numerical investigation of compressor tandem aerofoils featuring near-endwall modification," *J. Phys.: Conf. Ser.* **1909**, 012019 (2021).
- ¹¹A. Kumar and A. M. Pradeep, "Response of a tandem-staged compressor to circumferential inflow distortion," *ASME J. Fluids Eng.* **144**(9), 091202 (2022).
- ¹²A. Kumar, H. Chhugani, S. More, and A. M. Pradeep, "Effect of differential tip clearance on the performance of a tandem rotor," *ASME J. Turbomach.* **144**(8), 081007 (2022).
- ¹³H. Liu, S. Yue, Y. Wang, and J. Zhang, "Unsteady study on the effects of matching characteristic of tandem cascade on the performance and flow at large angle of attack," *J. Therm. Sci.* **27**, 505–515 (2018).
- ¹⁴A. Kumar, A. Kumar, H. Chhugani, S. More, and A. M. Pradeep, "Understanding the effect of three-dimensional design in tandem blade," *ASME J. Turbomach.* **146**(3), 031002 (2024).
- ¹⁵S. Fathi, M. Boroomand, and H. Eshraghi, "Improving near-stall performance of axial flow compressors using variable rotor tandem stage. A steady analysis," *Phys. Fluids* **36**(9), 097101 (2024).
- ¹⁶S. Babu, P. Chatterjee, and A. M. Pradeep, "Transient nature of secondary vortices in an axial compressor stage with a tandem rotor," *Phys. Fluids* **34**(6), 065125 (2022).
- ¹⁷M. Hewkin-Smith, G. Pullan, S. D. Grimshaw, E. M. Greitzer, and Z. S. Spakovszky, "The role of tip leakage flow in spike-type rotating stall inception," *ASME J. Turbomach.* **141**(6), 061010 (2019).
- ¹⁸G. Pullan, A. M. Young, I. J. Day, E. M. Greitzer, and Z. S. Spakovszky, "Origins and structure of spike-type rotating stall," *ASME J. Turbomach.* **137**(5), 051007 (2015).
- ¹⁹H. D. Vo, C. S. Tan, and E. M. Greitzer, "Criteria for spike initiated rotating stall," *ASME J. Turbomach.* **130**(1), 011023 (2008).
- ²⁰K. Yamada, H. Kikuta, K. Iwakiri, M. Furukawa, and S. Gunjishima, "An explanation for flow features of spike-type stall inception in an axial compressor rotor," *ASME J. Turbomach.* **135**(2), 021023 (2013).
- ²¹H. Wang, Y. Wu, and H. Ouyang, "Numerical investigations of rotating instability and unsteady tip vortex structures in an axial compressor," in *Turbo Expo: Power for Land, Sea, and Air* (American Society of Mechanical Engineers, 2018), Vol. 50992, p. V02AT45A031.
- ²²Z. Chen, Y. Wu, and G. An, "Tip leakage flow, tip aerodynamic loading and rotating instability in a subsonic high-speed axial flow compressor rotor," *Aerosp. Sci. Technol.* **110**, 106486 (2021).
- ²³H. Khaleghi, "Stall inception and control in a transonic fan, part A: Rotating stall inception," *Aerosp. Sci. Technol.* **41**, 250–258 (2015).
- ²⁴T. Li, Y. Wu, and H. Ouyang, "Numerical investigation of tip clearance effects on rotating instability of a low-speed compressor," *Aerosp. Sci. Technol.* **111**, 106540 (2021).
- ²⁵H. Iim, X. Y. Chen, and G. Zha, "Detached-eddy simulation of rotating stall inception for a full-annulus transonic rotor," *J. Propul. Power* **28**(4), 782–798 (2012).
- ²⁶B. Wang, Y. Wu, F. Yang, and S. Spence, "Intermittent breakdown of the tip leakage vortex and the resultant flow unsteadiness in the tip-region of a subsonic compressor cascade," *Aerosp. Sci. Technol.* **113**, 106679 (2021).
- ²⁷I. Day, "Stall inception in axial flow compressors," *ASME J. Turbomach.* **115**(1), 1–9 (1993).
- ²⁸T. R. Camp and I. J. Day, "A study of spike and modal stall phenomena in a low-speed axial compressor," in *Proceedings of the ASME 1997 International Gas Turbine and Aeroengine Congress and Exhibition. Volume 1: Aircraft Engine; Marine; Turbomachinery; Microturbines and Small Turbomachinery, Orlando, Florida, USA* (ASME, 1997), p. V001T03A109.
- ²⁹J. Dodds and M. Vahdati, "Rotating stall observations in a high speed compressor—Part I: Experimental study," *ASME J. Turbomach.* **137**(5), 051002 (2015).
- ³⁰J. Dodds and M. Vahdati, "Rotating stall observations in a high speed compressor—Part II: Numerical study," *ASME J. Turbomach.* **137**(5), 051003 (2015).
- ³¹A. D. Gardner, A. R. Jones, K. Mulleners, J. W. Naughton, and M. J. Smith, "Review of rotating wing dynamic stall: Experiments and flow control," *Prog. Aerosp. Sci.* **137**, 100887 (2023).
- ³²Z. Li, D. Zhang, Y. Liu, A. Azma, and N. Gao, "On the unsteady wake flow behind a sphere with large transverse-rotating speeds," *Phys. Fluids* **35**(10), 105127 (2023).
- ³³L. Chen, C. Cheng, C. Zhou, Y. Zhang, and J. Wu, "Flapping rotary wing: A novel low-Reynolds number layout merging bionic features into micro rotors," *Prog. Aerosp. Sci.* **146**, 100984 (2024).
- ³⁴I. Ansys, *CFX-Solver Theory Guide, Release 2023 R2* (ANSYS, Inc., 2023).
- ³⁵M. Inoue and M. Kuroumaru, "Structure of tip clearance flow in an isolated axial compressor rotor," *ASME J. Turbomach.* **111**(3), 250–256 (1989).
- ³⁶N. M. McDougall, "A comparison between the design point and near stall performance of an axial compressor," *ASME J. Turbomach.* **112**(3), 109–115 (1990).
- ³⁷F. Yang, Y. Wu, S. Spence, B. Li, and Z. Chen, "The investigation on vortex breakdown prior to stall in a compressor rotor with non-uniform tip clearance," *Phys. Fluids* **36**(8), 084120 (2024).